Lead-Free Piezoceramics

Ergodic and Nonergodic Relaxor Ferroelectrics Based on Bismuth Sodium Titanate

Vom Fachbereich Material- und Geowissenschaften zur Erlangung des akademischen Grades Doktor-Ingenieur (Dr.-Ing.) genehmigte Dissertation von Dipl.-Ing. Robert Dittmer aus Dessau-Roßlau

April 2013 — Darmstadt — D 17

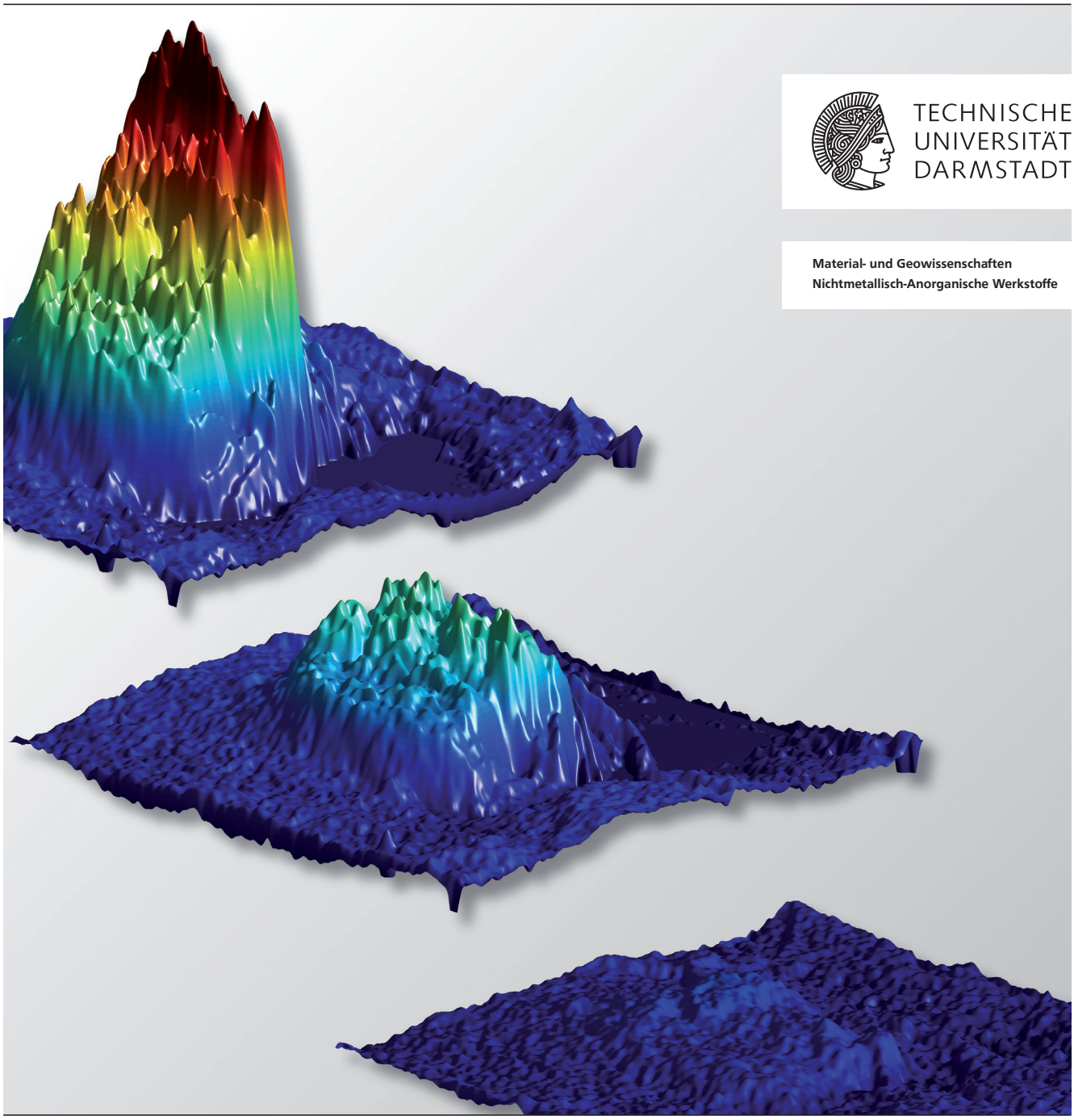

TECHNISCHE UNIVERSITÄT DARMSTADT

Material- und Geowissenschaften
Nichtmetallisch-Anorganische Werkstoffe

Lead-Free Piezoceramics – Ergodic and Nonergodic Relaxor Ferroelectrics Based on Bismuth Sodium Titanate

Vorgelegte Dissertation von Robert Dittmer aus Dessau-Roßlau

1. Gutachten: Prof. Dr.-Ing. Jürgen Rödel

2. Gutachten: Prof. Dr. rer. nat. Karsten Albe

Tag der Einreichung: 23. April 2013
Tag der Verteidigung: 19. Juni 2013

Darmstadt, 2013 — D 17

"The important thing is not to stop questioning.

Curiosity has its own reason for existing."

Albert Einstein

Contents

Symbols and Abbreviations

Symbols

A	Area of the electrode
A	Fitting parameter (factor)
A	Amplitude of piezoresponse (PFM)
A_0	Amplitude at resonance frequency (PFM)
a	Landau coefficient
a	Lattice parameter
α	Polarizability
α_{el}	Electronic polarizability
b	Fitting parameter (exponent)
b	Sample width
b	Landau coefficient
b	Lattice parameter
β	Stretching exponent
C	Capacitance
C	Landau coefficient
c^E	Stiffness at constant electric field
C_m	Measurement capacitance
C_s	Sample capacitance
C_{vol}	Volumetric heat capacity
χ	Electric susceptibility
$\boldsymbol{D}$	Dielectric displacement vector
d_{33}	Piezoelectric coefficient measured along the poling direction
d^*_{33}	Normalized strain $S_{max}{\cdot}E^{-1}_{max}$
$d_{33,0}$	Piezoelectric coefficient at electric zero-field
$d_{33,6}$	Piezoelectric coefficient at maximum applied electric field of 6 kV·mm^{-1}
d_{ijk}	Piezoelectric tensor
d_{PFM}	Piezoresponse signal (PFM)
$\Delta Q/Q$	Instrumental resolution in diffraction
E	Electric field
$\boldsymbol{E}$	Electric field vector
$\boldsymbol{E'}$	Local Electric field vector
E_a	Activation Energy
$E_{inflection}$	Field of inflection point in $S(E)$
e_{loss}	Polarization loss density
E_{max}	Maximum applied electric field
E_a	Activation energy
E_c	Coercive field

$E_{c,-}$	Negative coercive field
$E_{c,+}$	Positive coercive field
e_P	Polarization energy density
ε'	Real part of the permittivity
ε''	Imaginary part of the permittivity
ε_0	Permittivity of the vacuum
ε_r	Relative permittivity
ε_1	Relative permittivity of dielectric 1
ε_2	Relative permittivity of dielectric 2
$\varepsilon_{r,33}$	Relative permittivity measured along the direction of field application
ε_{ik}	Dielectric tensor
f	Frequency
F	Free Energy
f_0	Attempt frequency in Vogel-Fulcher equation
F_0	Free energy of the reference state
F_b	Blocking force
f_R	Resonance frequency
$F(x, P)$	Free energy function
G	Shear modulus
h_i	Term describing quenched random fields
η^*	Efficiency factor
$I_{SHG,norm}$	Normalized SHG intensity
I_i	Dipole moments
I_j	Dipole moments
J_{ij}	Term describing random bonds
k	Boltzmann constant
k_{33}	Coupling factor for longitudinal oscillation
k_t	Coupling factor for thickness oscillation
k_p	Coupling factor for radial oscillation of a thin plate
K_{uni}	Uniaxial compressive modulus
L	Sample length
l_c	Coherence length (SHG)
λ	Wavelength
m	Sample mass
M_{ijkl}	Electrostrictive tensor (field-dependent notation)
n_ω	Refractive index at incident frequency (SHG)
$n_{2\omega}$	Refractive index at doubled frequency (SHG)
ω	Laser frequency (SHG)
P	Polarization
$\boldsymbol{P}$	Polarization vector
$\boldsymbol{p_{av}}$	Average dipole moment
P_{max}	Polarization at maximum electric field
P_{rem}	Remanent polarization at electric zero-field

$P_{rem,+}$	Positive remanent polarization
$P_{rem,-}$	Negative remanent polarization
P_{sw}	Switching polarization (PFM)
P_s	Spontaneous polarization
ϕ	Phase angle
π_i	Pyroelectric coefficient
Q	Quality factor
Q	Charge
Q_{ijkl}	Electrostrictive tensor (polarization-dependent notation)
Q_{ij}	Electrostrictive matrix (Voigt notation)
Q_{11}	Longitudinal electrostrictive coefficient (Voigt notation)
Q_{12}	Transverse electrostrictive coefficient (Voigt notation)
Q_m	Charge on measurement capacitor
Q_s	Charge on sample surface
Q_0	Initial charge of a capacitor
R^2	Coefficient of determination
r_c	Correlation length
RC	Time constant, figure of merit for capacitors
ρ	Electrical resistivity
S	Strain
S_3	Strain measured along the direction of applied electric field
s_{33}^D	Elastic compliance along poling direction under open-circuit conditions (Voigt notation)
s_{33}^E	Elastic compliance along poling direction under short-circuit conditions (Voigt notation)
S_{ij}	Strain tensor
s_{ijkl}^E	Elastic compliance tensor at constant electric field
s_{eff}	Effective particle size (SHG)
S_f	Free strain
S_{max}	Maximum strain
S_{neg}	Negative strain
S_{pol}	Poling strain
S_{rem}	Remanent strain
σ_b	Blocking stress
$\sigma_{el,1}$	Electrical conductivity of dielectric 1
$\sigma_{el,2}$	Electrical conductivity of dielectric 2
σ_{kl}	Stress tensor
σ_{peak}	Stress where field-induced maximum polarization or strain peak
t	Sample thickness
t	Time
T	Temperature
T_0	Curie-Weiss temperature
T_B	Burns Temperature
T_c	Transition temperature
T_{c0}	Transition temperature during zero-field heating

T_d	Depolarization temperature determined from $d_{33}(T)$
T_f	Freezing temperature
$T_{F\text{-}R}$	Ferroelectric to relaxor temperature determined from $\varepsilon(T)$
T_l	Correction factor in calculation of Young's modulus
T_m	Temperature of maximum permittivity
$T_{onset,1}$	Lower onset temperature of $Y(T)$ curves
$T_{onset,2}$	Upper onset temperature of $Y(T)$ curves
tanδ	Loss tangent
τ	Relaxation time
τ_{MW}	Maxwell-Wagner relaxation time
θ	Diffraction angle
U	Voltage
U_m	Voltage drop across measurement capacitance
w	Scan width (PFM)
U_{sw}	Switching voltage
$U_{sw,-}$	Negative switching voltage (PFM)
$U_{sw,+}$	Positive switching voltage (PFM)
w	Mechanical work output density
w_{max}	Maximum mechanical work output density
x	Mole fraction of second compound in a pseudo-ternary solid solution
ξ	Angle between applied electric field and diffraction scattering vector
Y	Young's modulus (elastic measurement)
y	Mole fraction of third compound in a pseudo-ternary solid solution
y_0	Offset fitting parameter in stretched exponential function (PFM)
y_1	Fitting parameter in stretched exponential function (PFM)

Abbreviations

AC	Alternating current
AFE	Antiferroelectric
AFM	Atomic force microscopy
BA	Bismuth aluminate $BiAlO_3$
BAgT	Bismuth silver titanate $Bi_{1/2}Ag_{1/2}TiO_3$
BC	Bismuth cobalt oxide $BiCoO_3$
BCr	Bismuth chromium oxide $BiCrO_3$
BE	Band excitation (PFM)
BF	Bismuth ferrite $BiFeO_3$
BH	Barium hafnate $BaHfO_3$
BKT	Bismuth potassium titanate $Bi_{1/2}K_{1/2}TiO_3$
BLA	Bismuth lanthanum aluminate $Bi_{1/2}La_{1/2}AlO_3$
BLT	Bismuth lithiumate titanate $Bi_{1/2}Li_{1/2}TiO_3$

BMT	Bismuth magnesate titanate $BiMg_{1/2}Ti_{1/2}O_3$
BNiT	Bismuth niccolate titanate $BiNi_{1/2}Ti_{1/2}O_3$
BNT	Bismuth sodium titanate $Bi_{1/2}Na_{1/2}TiO_3$
BNT-100xBKT-100yBZT	(1-y)((1-x)$Bi_{1/2}Na_{1/2}TiO_3$ – $x Bi_{1/2}K_{1/2}TiO_3$) – $y BiZn_{1/2}Ti_{1/2}O_3$
BNT-6BT-100yKNN	(1-y)(0.94$Bi_{1/2}Na_{1/2}TiO_3$ – 0.06$BaTiO_3$) – $y K_{0.5}Na_{0.5}NbO_3$
BT	Barium titanate $BaTiO_3$
BZr	Barium zirconate $BaZrO_3$
DART	Dual AC Resonance Tracking
DC	Direct current
DMA	Dynamic Mechanical Analysis/Analyzer
DSC	Differential scanning calorimetry
ER	Ergodic relaxor
ESRF	European Synchrotron Radiation Facility
FC	Field cooling
FE	Ferroelectric
HRTEM	High-resolution TEM
HTE	High-temperature electronics
IP	In-plane (PFM)
IR	Infrared
KNN	Potassium sodium niobate $K_{0.5}Na_{0.5}NbO_3$
MPB	Morphotropic phase boundary
NR	Nonergodic relaxor
NRD	Neutron diffraction
OP	Out-of-plane (PFM)
PE	Paraelectric
PFM	Piezoresponse force microscopy
PFN	Lead ferrate niobate $Pb(Fe_{1/2}Nb_{1/2})O_3$
PIN	Lead indiumate niobate $Pb(In_{1/2}Nb_{1/2})O_3$
PLZT	Lanthanum-modified lead zirconate titanate $(Pb_{1-x}La_x)(Zr_{1-y}Ti_y)O_3$
PMN	Lead magnesium niobate $Pb(Mg_{1/3}Nb_{2/3})O_3$
PMT	Lead manganate tantalate $Pb(Mn_{1/3}Ta_{2/3})O_3$
PNR	Polar nano-region
PSN	Lead scandate niobate $Pb(Sc_{1/2}Nb_{1/2})O_3$
PST	Lead scandate tantalate $Pb(Sc_{1/2}Ta_{1/2})O_3$
PT	Lead titanate $PbTiO_3$
PTFE	Polytetrafluoroethylene
PZN	Lead zinc niobate $Pb(Zn_{1/3}Nb_{2/3})O_3$
PZT	Lead zirconate titanate $Pb(Zr_{1-y}Ti_y)O_3$
RF	Relaxor ferroelectric
R/T	Rhombohedral and tetragonal phase mixture
SBN	Strontium barium niobate $Sr_xBa_{1-x}Nb_2O_6$
SHG	Second-harmonic generation
SHO	Single harmonic oscillator

ST	Strontium titanate $SrTiO_3$
TEM	Transmission electron microscopy
TSDC	Thermally-stimulated depolarization current
UV	Ultraviolet radiation
vis	Visible light
XRD	X-ray diffraction
ZFC	Zero-field cooling

1 Introduction

In light of diminishing global resources, one of the most demanding challenges of the 21st century is the increase of efficiency with regard to materials and energy. In order to accomplish this goal it requires innovative and high-performance materials and concepts. One of the key components in this quest is multifunctional materials that are capable of transforming energy. In this context, piezoelectrics are particularly attractive, allowing practically instantaneous conversion of mechanical energy into electrical energy and *vice versa*. This extraordinary feature allows, for example, precisely timed high-pressure injection of fuel, thereby improving the overall efficiency of an automotive by up to 20 %.[1] Another promising field of application for piezoelectrics are smart systems, often also referred to as adaptronics. The integration and elaborated interplay between actuators and sensors affords a multitude of possibilities, *e.g.*, shape control, ultra-precise positioning, health monitoring as well as the damping of vibration and noise.[2] Therefore, piezoelectrics contribute to light-weight design and overall system efficiency by superseding otherwise necessary stiffening or damping elements. The predominant piezoelectric material of choice is lead zirconate titanate $PbZr_xTi_{1-x}O_3$ (PZT). Since the first reports in the 1950s,[3,4] its properties have gradually evolved with optimized chemistry, microstructure, and processing technology.

Against the background of increasing environmental awareness, the distribution of lead-containing devices throughout consumer products faces increasing restrictions due to ecological and health concerns. For this reason, there are international attempts to reduce the amount of hazardous substances through legislation.[5] This development triggered extensive research efforts to find lead-free alternatives to PZT. This step is a noteworthy attempt towards rendering this technology more environment-friendly and sustainable. The political will behind this evolution, however, is also a much needed stimulus to explore new material concepts and to dare to go beyond PZT – a material, which has, after all, dominated the market for almost 60 years. Despite incremental improvements, the piezoceramics field is waiting to be revolutionized, like when barium titanate was replaced by the vastly superior PZT.

Despite several promising findings in recent years, it has become evident that one single compound will likely not replace lead-containing materials across the whole diverse range of applications. Rather, multiple, tailored lead-free solutions are sought for individual applications. In the case of actuation, where large displacements are required, pseudobinary and -ternary solid solutions based on $Bi_{1/2}Na_{1/2}TiO_3$ (BNT) were reported to provide outstanding electromechanical performance – partially competing with or even surpassing PZT. This class of materials is appealing not just from an application point of view but also from a scientific perspective; the peculiar field-dependent behavior and the underlying physical mechanism for the observed large strain have long been unexplained. First, a number of hypotheses involved antiferroelectricity and field-induced phase transitions. However, our understanding has greatly evolved since then. Furthermore, the mystery surrounding these materials is not limited to the field-dependent behavior but also extends to the thermal evolution of both structure and properties as well as the interplay between both. Moreover, questions relevant for a comprehensive evaluation of these materials are currently unanswered, for

example: Is the underlying strain mechanism robust enough to also sustain high driving frequencies or uniaxial mechanical loads?

The objective of the present work is to discuss and clarify fundamental issues related to this class of BNT-based lead-free piezoelectrics. For this purpose, two material systems, (1-y)(0.94$Bi_{1/2}Na_{1/2}TiO_3$-0.06$BaTiO_3$)-$yK_{0.5}Na_{0.5}NbO_3$ (BNT-6BT-100yKNN) and (1-y)((1-x)$Bi_{1/2}Na_{1/2}TiO_3$-$xBi_{1/2}K_{1/2}TiO_3$)-$yBiZn_{1/2}Ti_{1/2}O_3$ (BNT-100xBKT-100yBZT), are investigated with respect to their electrical, structural, microstructural, and mechanical properties with electric field, temperature, stress, and composition as the main variables. This systematic and broad methodological approach grants deep insight into the fundamental mechanisms, spanning multiple length scales from a submicroscopic to a macroscopic point of view. By direct comparison of both systems, fundamental and universally valid interrelationships shall be elaborated and contrasted with well-studied lead-containing materials. Beyond the primary focus on the mechanistic discussion, these materials and their modifications will finally be evaluated and classified with respect to actual applications, not only for actuation but also as dielectric materials in high-capacity, high-temperature capacitors.

2 Theory and Literature Review

This chapter summarizes the most important fundamental concepts required for the description and understanding of the lead-free piezoceramics as discussed in the present work. The first part revisits dielectrics, ranging from basics on polarization mechanisms to theories on relaxor ferroelectrics. Later sections will elucidate materials of importance for this work, namely bismuth sodium titanate and its derived pseudobinary and -ternary compositions. A concise selection of the most essential research articles is referenced in this chapter.

2.1 Properties of Dielectrics

2.1.1 Fundamental Characteristics

Dielectrics and Involved Polarization Mechanisms

The following description of dielectrics is based upon the text books of Moulson[6] and Waser *et al.*.[7]

All electrical insulators are dielectrics with a polarization arising from the interaction of the matter with an electric field.[1] As ceramics are in general electrically non-conductive materials with a high band gap, they are polarized under the influence of an electric field. The macroscopic polarization $\boldsymbol{P}$ is the sum of all dipole moments related to a unit volume. The proportionality factor that interrelates the macroscopic polarization and the external electric field $\boldsymbol{E}$ is the dielectric susceptibility χ according to the following equation

$$\boldsymbol{P} = \varepsilon_0 \cdot \chi \cdot \boldsymbol{E} \tag{2.1}$$

where ε_0 is the permittivity of the vacuum. Polarization and the dielectric displacement $\boldsymbol{D}$ are interrelated as follows.

$$\boldsymbol{D} = \varepsilon_0 \boldsymbol{E} + \boldsymbol{P} \tag{2.2}$$

The dielectric susceptibility can furthermore be expressed by means of the relative dielectric constant ε_r

$$\chi = \varepsilon_r - 1. \tag{2.3}$$

Despite what the term "dielectric constant" may suggest, ε_r is not constant but may strongly vary upon changes of factors such as temperature, electric field, stress, or measurement frequency.

On a microscopic scale, the effect of an electric field on a dielectric is described by means of dipole moments. The average dipole moment $\boldsymbol{p_{av}}$ of the dielectric is proportional to the applied

[1] Please note that within this work the term 'field' will always refer to the electric field unless stated otherwise.

electric field with the polarizability α interrelating $\boldsymbol{p_{av}}$ and the local electric field vector $\boldsymbol{E'}$, as illustrated by Equation 2.4.

$$\boldsymbol{p_{av}} = \alpha \cdot \boldsymbol{E'} \tag{2.4}$$

The polarizability involves distinct contributions as schematically illustrated by Figure 2.1.

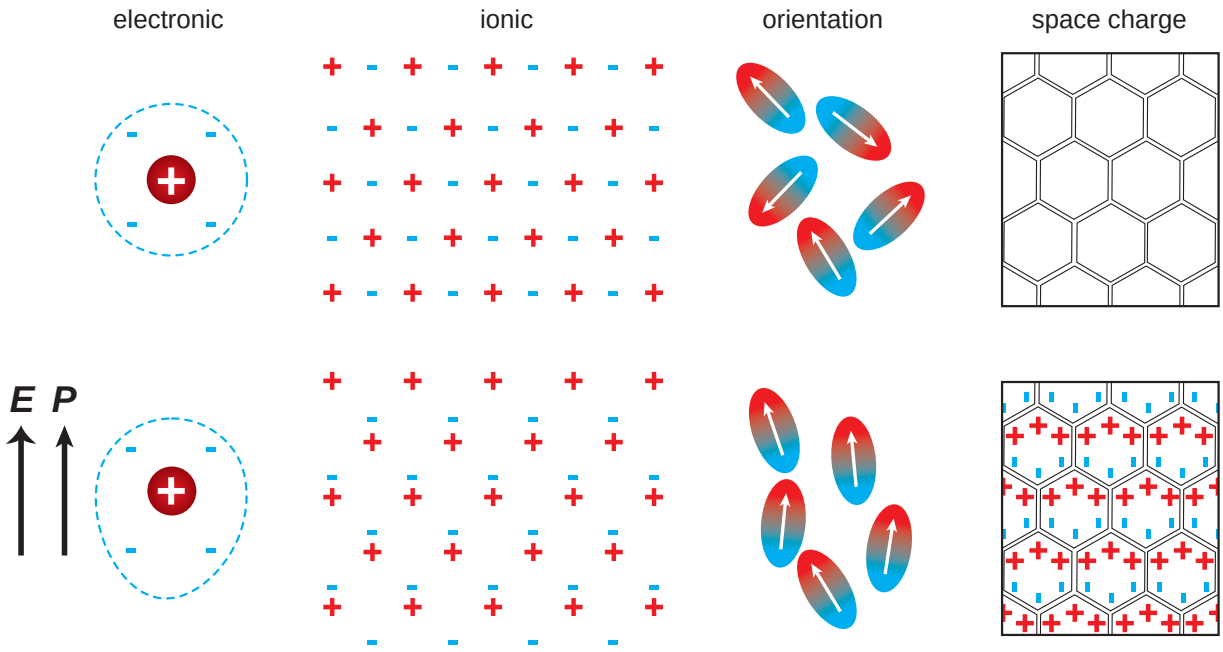

Figure 2.1: Distinct microscopic polarization mechanisms (after Ref. [7]).

The displacement of negatively charged electrons with respect to the positively charged core is referred to as electronic polarization and occurs in all dielectrics. Since the electronic polarizability α_{el} is in first approximation proportional to the volume of the electron shell, large atoms usually have a large electronic polarizability. Ionic crystals may furthermore exhibit an ionic polarization emerging from the field-driven displacement of positively charged cations against negatively charged anions. Orientation polarization is the field-induced alignment of permanent dipoles, which would otherwise exhibit a statistical distribution of the dipole moments in the absence of an electric field. Space charge polarization may be observed in dielectrics with inhomogeneously distributed charge carrier densities.

A special case is the Maxwell-Wagner[8,9] polarization. This interfacial polarization occurs at the heterogeneous boundary between two dielectrics due to distinct conductivities, which give rise to a pile-up of charges at that interface. In the case of ceramics the Maxwell-Wagner polarization may occur on a mesoscopic scale between grains and grain boundaries as well as on a macroscopic scale at the electrode-sample interface. It is interesting to note that this effect creates a time or frequency dependence of the polarization, referred to as Maxwell-Wagner relaxation with the relaxation time τ_{MW}. For the model case of two dielectrics with permittivity ε_1, ε_2 and electrical

conductivity $\sigma_{el,1}$, $\sigma_{el,2}$ the relaxation time is calculated as given by Equation 2.5.

$$\tau_{MW} = \varepsilon_0 \cdot \frac{\varepsilon_1 + \varepsilon_2}{\sigma_{el,1} + \sigma_{el,2}} \tag{2.5}$$

As illustrated by Figure 2.2, space charge relaxation is observed at low frequencies corresponding to long radio wavelengths, whereas the other mechanisms disappear at significantly higher frequency ranges.

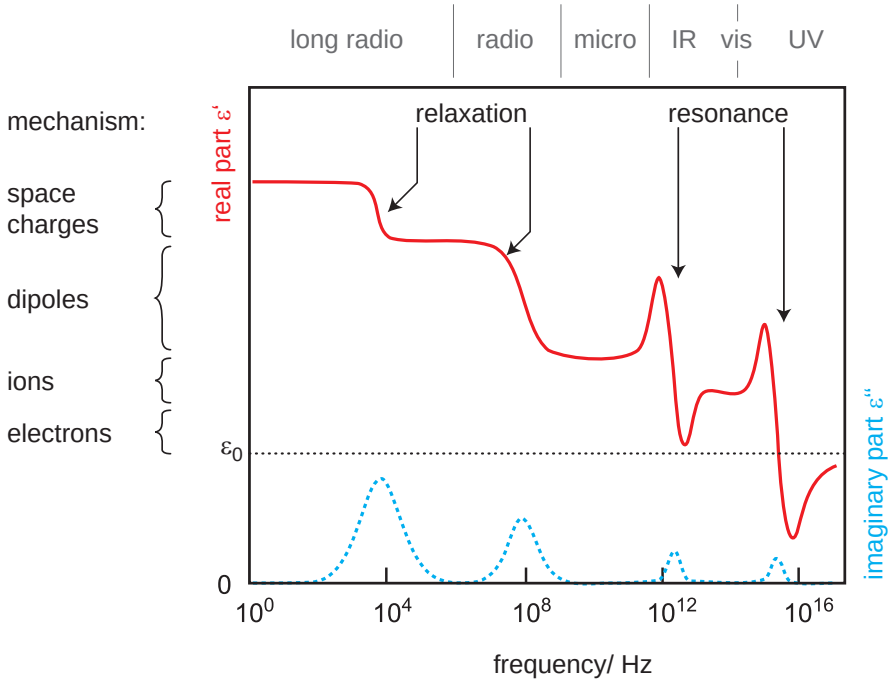

Figure 2.2: Schematic of the principal frequency dependence of the real and imaginary part of permittivity. Top: respective wavelength range according to the electromagnetic spectrum: long radio waves, radio waves, microwaves, infrared (IR) radiation, visible light (vis), ultraviolett (UV) radiation (after Ref. [7]).

Another factor to the overall polarizability involves domain walls, which will be introduced later.

All dielectrics exhibit a field-induced strain.[10] From the free energy function $F(x, P)$ of an unstrained, unpolarized crystal the strain S_{ij} for a non-centrosymmetric system can be shown to be

$$S_{ij} = -s^E_{ijkl}\sigma_{kl} + M_{ijkl}E_kE_l \tag{2.6}$$

with strain S_{ij}, elastic compliance s^E_{ijkl}, electric field E_k and E_l, stress σ_{kl} and the electrostrictive tensor M_{ijkl}.[11] The strain S depends on E^2 and, therefore, is always independent of the polarity of the excitation field. A figurative explanation for the occurrence of electrostrictive strain was given by Uchino.[12] The imaginary springs, which symbolize bonding forces between ions, are not ideal, but possess anharmonicity, that is, the spring constant in tension is larger than in compression. Because of that, an electric field will induce a strain that is independent of the direction

of the electric field. In nonlinear dielectric ceramics, the strain is often expressed as a function of polarization squared, related by the electrostrictive tensor Q_{ijkl} according to the following equation.

$$S_{ij} = Q_{ijkl} P_k P_l \tag{2.7}$$

As in the prototypical electrostrictor (1-x)Pb($Mg_{1/3}Nb_{2/3}$)O_3-$x$$PbTiO_3$ (PMN-100xPT) depicted in Figure 2.3, the electrostrictive coefficient Q_{ij} (Voigt notation) can consequently be determined from the slope of the linear branches of the strain curve plotted against polarization squared. The Q_{11} parameter describes longitudinal strain whereas Q_{12} describes transverse strain with respect to the polarization direction.

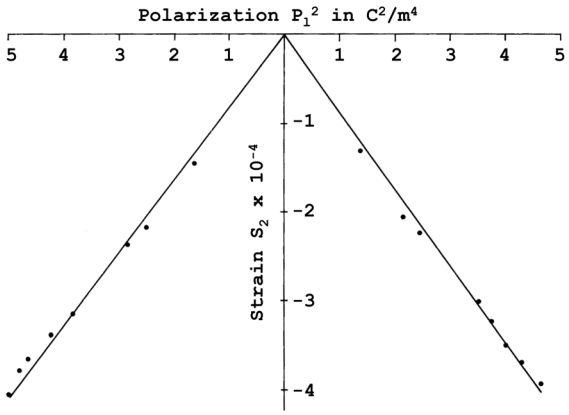

Figure 2.3: Strain as a function of polarization squared for 0.9PMN-0.1PT (Ref. [13]).

Polar Dielectrics

As depicted by Figure 2.4, piezoelectrics are a subgroup of dielectrics. They are characterized by a linear coupling between electrical and mechanical energy. From a total of 32 crystallographic point groups, 21 are non-centrosymmetric, a necessary condition for being piezoelectric (see Table 2.1 for an overview of point groups). Out of these 21 point groups, piezoelectricity can be observed in all but the point group 432.

Piezoelectricity may be defined by means of the following two equations

$$D_i = d_{ijk} \cdot \sigma_{jk} + \varepsilon^{\sigma}_{ik} \cdot E_k \tag{2.8}$$

$$S_{ij} = s^{E}_{ijkl} \cdot \sigma_{kl} + d_{ijk} \cdot E_i \tag{2.9}$$

Equation 2.8 describes the direct piezoelectric effect. The dielectric displacement D_i is coupled to the stress σ_{jk} via the piezoelectric tensor d_{ijk}. There is furthermore a second, dielectric contribution from the permittivity ε_{ik} at an electric field E_k. The converse effect is described by Equation 2.9 where strain S_{ij} is coupled to the electric field E_i via d_{ijk}. In addition, there is an elastic contribution to strain described by the Hooke's law with the compliance s^{E}_{ijkl} and the stress σ_{kl}.

From the 21 point groups that are not centrosymmetric, 10 display a spontaneous polarization P_s, meaning that the centers of the positive and negative charges do not coincide. Due to the

Table 2.1: Overview on crystallographic point groups in short Hermann-Mauguin nomenclature (after Ref. [14]).

centrosymmetry		centrosymmetric	non-centrosymmetric	
polarity		non-polar	non-polar	polar
number of point groups		11	11	10
crystal class	cubic	$m\bar{3}m$, $m\bar{3}$	432, $\bar{4}3m$, 23	
	hexagonal	$6/mmm$, $6/m$	622, $\bar{6}m2$, $\bar{6}$	$6mm$, 6
	tetragonal	$4/mmm$, $4/m$	422, $\bar{4}2m$, $\bar{4}$	$4mm$, 4
	rhombohedral	$\bar{3}m$, $\bar{3}$	32	$3m$, 3
	orthorhombic	mmm	222	$mm2$
	monoclinic	$2/m$		2, m
	triclinic	$\bar{1}$		1

temperature dependence of P_s, changes in temperature affect the density of charges at the surface of the crystal. This effect is referred to as pyroelectricity with the pyroelectric coefficient $\pi_i = \partial P_{s,i} \cdot \partial T^{-1}$.

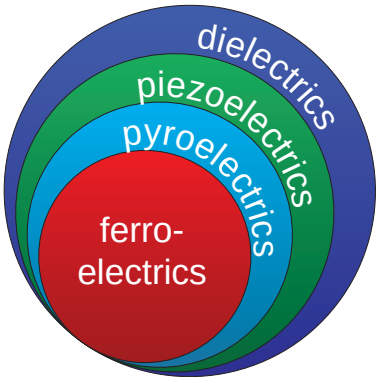

Figure 2.4: Classification of dielectrics.

Ferroelectrics are dielectric materials that exhibit both the piezoelectric and the pyroelectric effect as illustrated by Figure 2.4. Importantly, ferroelectrics possess at least two energetically equivalent spontaneous polarization directions, where the local polarization of the crystal can be reoriented between these states by means of an external electric field. This has invaluable practical implications. Not only single-crystals but also ferroelectric polycrystals can exhibit a macroscopically measurable piezo- and pyroelectric effect. A macroscopic net non-zero polarization is created by application of a sufficiently high electric field that gives rise to a preferential alignment of the initially randomly oriented individual P_s vectors. The most important features of ferroelectrics are briefly presented in the next section, followed by a description of relaxor ferroelectricity, a phenomenon closely related yet substantially different from conventional ferroelectricity.

2.1.2 Ferroelectrics

If not stated otherwise, the references within this chapter are the review articles by Hall[15] and Damjanovic[16] and the textbooks or book chapters by Jaffe,[17] Lines and Glass,[18] Ruschmeyer,[19] and Waser.[7]

A definition of ferroelectricity, first discovered in Seignette salt,[20] was proposed by Jaffe:[21]

"*The ability of certain crystals of electrically polar structure to switch the direction of polarity under the influence of a strong electrical field between several crystallographically equivalent directions and to retain their new orientation after removal of the field.*"

The polar structure, implying a spontaneous polarization, is in most practically relevant materials a non-cubically distorted ABO_3 perovskite structure as in the case of the prototype ferroelectric ceramic barium titanate, $BaTiO_3$ (BT).[22] Using the example of barium titanate, both the perovskite structure and phase transitions will be summarized in the following.

Ferroelectric Phase Transitions

The high-temperature barium titanate polymorph is cubic with the large barium cation Ba^{2+} on the A-site, the smaller titanium cation Ti^{4+} on the B-site, and oxygen anions O^{2-} in the face centers as illustrated by Figure 2.5.[23] Since the center of both positive and negative charges coincide, BT is paraelectric (PE) at temperatures beyond the transition temperature T_c=128 °C.[24] [2]

Eventually, upon cooling, a phase transition from a cubic paraelectric to a tetragonal ferroelectric phase is observed (see Figure 2.5). The tetragonal distortion is associated with the creation of a spontaneous polarization. A thermodynamic description of this transition can be provided by means of the Landau-Devonshire theory.[27] In the case of one polar axis the free energy F can be expressed by means of a Taylor series expansion in the order parameter P.[28]

$$\Delta F = F - F_0 = \underbrace{\frac{1}{2}aP^2 + \frac{1}{4}bP^4 + \frac{1}{6}cP^6}_{F_L} - EP \tag{2.10}$$

Note that higher order terms are neglected while odd order terms are zero for reasons of symmetry. In this equation, a, b, and c are the Landau coefficients and F_0 is the energy of the reference state, typically taken to be the paraelectric phase. The minimum of ΔF determines the equilibrium state. The necessary and sufficient condition for such a minimum is provided by the first and the second partial derivative, respectively. The following equation applies.

$$\left.\frac{\Delta F}{\partial P}\right|_{P_0} = 0 \tag{2.11}$$

From 2.11 and 2.10 the following results from the Landau potential F_L.

$$\frac{\partial F_L}{\partial P} = E = P(a + bP^2 + cP^4) \tag{2.12}$$

[2] Note that T_c was shown to depend on particle size[25] as well as hydrostatic pressure.[26]

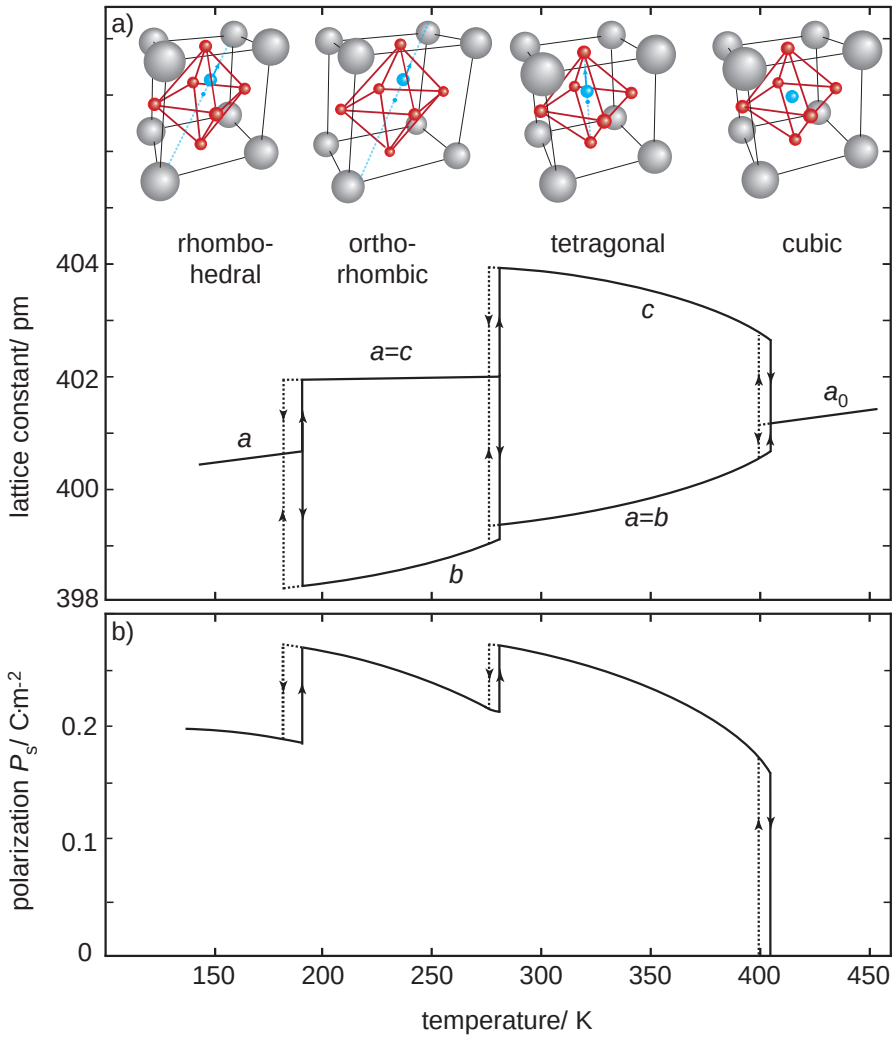

Figure 2.5: Schematic evolution of unit cell, lattice parameters, and spontaneous polarization of barium titanate (after Ref. [23]).

$$\frac{\partial^2 F_L}{\partial P^2} = \frac{1}{\chi} = a + 3bP^2 + 5cP^4 > 0 \tag{2.13}$$

In the paraelectric state P=0, resulting in the dielectric susceptibility of the paraelectric phase being

$$\chi = \frac{P}{E} = \frac{1}{a}. \tag{2.14}$$

Assuming a linear dependence of a on the temperature in the vicinity of the Curie-Weiss temperature T_0

$$a = a_0(T - T_0) \tag{2.15}$$

and further substitution of Equation 2.14 into Equation 2.15 and subsequent rearrangement yields the Curie-Weiss law.

$$\chi = \frac{C}{T - T_0} \tag{2.16}$$

Equation 2.16 describes the temperature dependence of the dielectric susceptibility in most ferroelectrics for the paraelectric phase, where T>T_0.

In the search for non-trivial solutions of Equation 2.12, two cases must be considered, namely a phase transition of first order with b<0 and a phase transition of second order with b>0.[7]

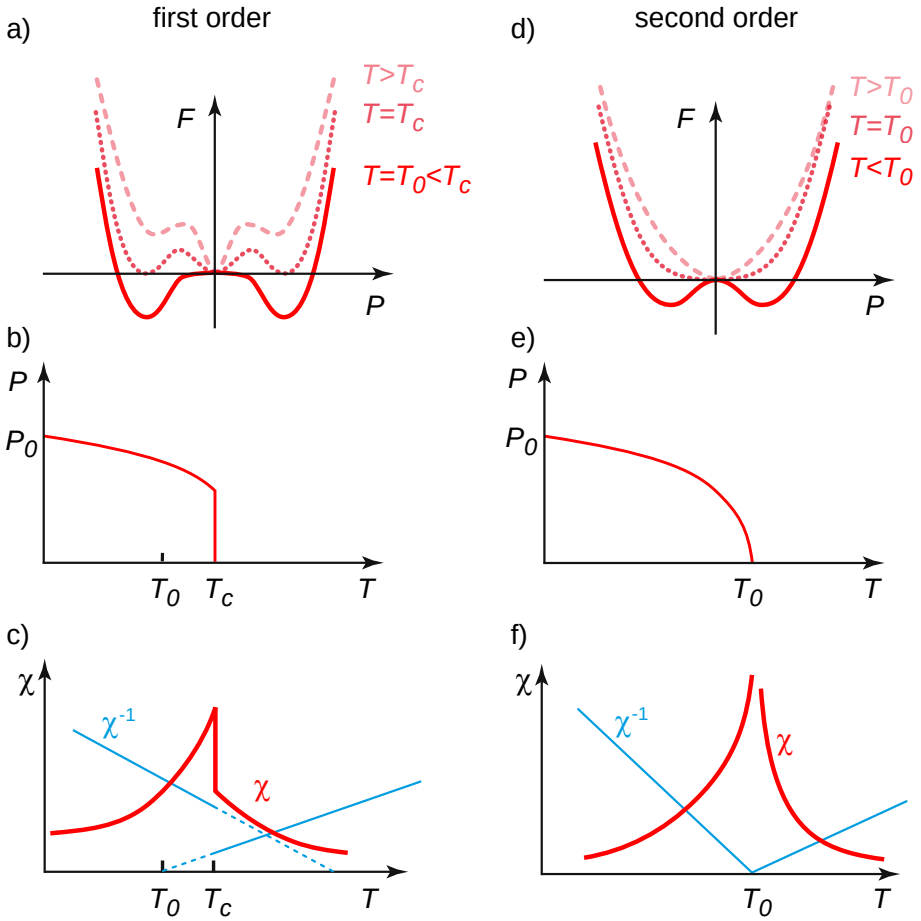

Figure 2.6: Free Energy $F(P)$, polarization $P(T)$, and susceptibility $\chi(T)$ for a first order (a, b, c) and a second order (d, e, f) phase transition for E=0 (after Ref. [28]).

In the first case the $F(P)$ curve exhibits a parabolic shape with one minimum for P=0, corresponding to the paraelectric state. Upon cooling, two additional secondary minima emerge but they are energetically unfavorable compared to P=0, as illustrated by Figure 2.6 a). At the transition temperature T_c, however, all three minima have the same energy. Upon further cooling F attains negative values, resulting in globally stable non-zero spontaneous polarization values. In the temperature range between T_c and T_0 the metastable paraelectric phase may still coexist next to the ferroelectric phase.[7] At a temperature between T_c and T_0, the first order phase transition takes place which is accompanied by a jump in P_s as well as a discontinuity in $\chi(T)$. The cubic to tetragonal transition in BT is a first order phase transition and so are the subsequent transitions to orthorhombic and rhombohedral symmetry as shown in Figure 2.5.[29]

For a second order transition, the high-temperature phase likewise features a parabolic free energy well with a minimum at P=0. Below the transition temperature T_c, which is equal to the Curie-Weiss temperature T_0, a spontaneous polarization develops, as schematically shown by the $F(P)$ curves in Figure 2.6 d). Hereby P_s changes continuously and is a function of the temperature difference with respect to T_0. While $P(T)$ follows a square root law (see Figure 2.6 e)), the temperature-dependent susceptibility exhibits a pole at T_0. Below T_0, the slope of the $\chi^{-1}(T)$ curve is two times the slope of $\chi^{-1}(T)$ above T_0 as, for example, demonstrated for the second order phase transition in lithium tantalate.[30]

Domains and Domain Switching

The spontaneous polarization developed in the ferroelectric phase of a single-domain single-crystal is accompanied by an apparent surface charge, which, in turn, gives rise to a depolarizing field E_D, as depicted by Figure 2.7.

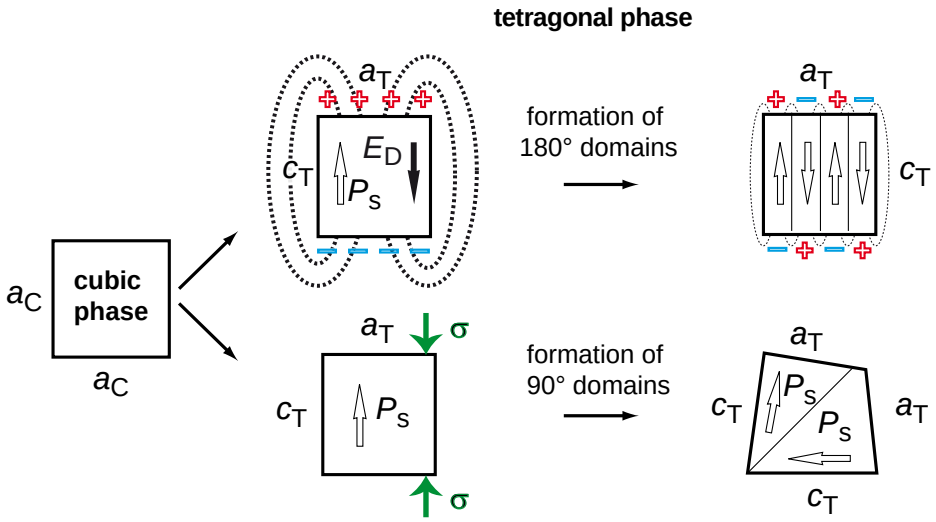

Figure 2.7: Schematic on the formation of 180 ° domains and 90 ° domains in a ferroelectric, tetragonal phase (after Ref. [31]).

The development of twinned domains occurs in order to minimize the electrostatic energy associated with this field; the crystal splits into regions of different polarization. These regions are referred to as 180 ° ferroelectric domains, separated by domain walls with a typical width of 1-10 nm. The twinning process is counteracted by the necessary energy involved in the creation of the domain walls. Moreover, non-180 ° domains are created in the presence of mechanical stress to minimize elastic energy (see Figure 2.7). Ferroelectric ceramics contain both 180 ° and non-180 ° domains because individual crystallites are subjected to local electric and mechanical stress fields. It is noted that only non-180 ° domain processes involve elastic deformations.

In addition to internal fields, external electric fields can also change the domain structure. This influence of the electric field is shown schematically together with a macroscopic polarization-electric field hysteresis loop in Figure 2.8. In the initial state (I), there is no net polarization as

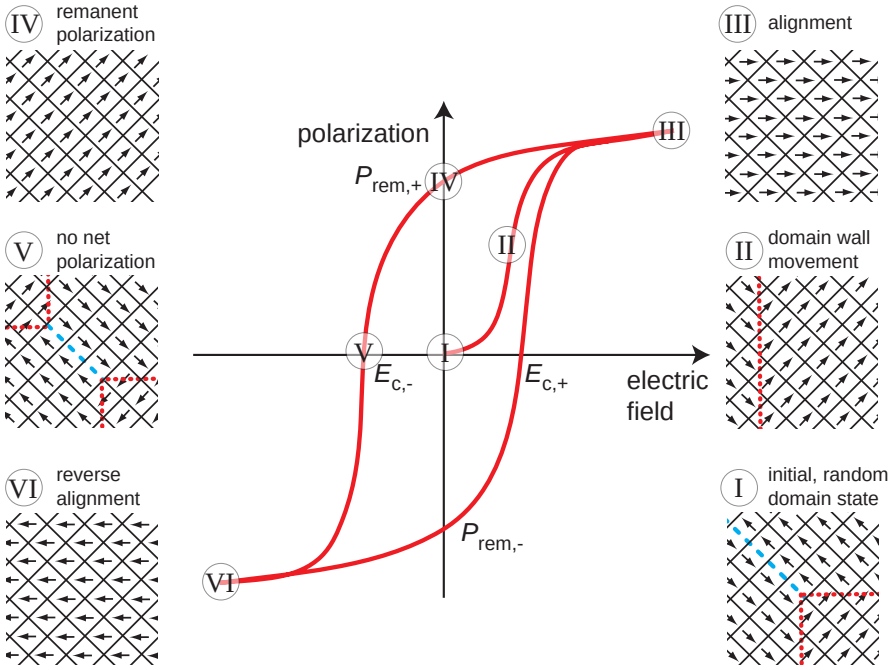

Figure 2.8: Polarization hysteresis $P(E)$ and concurrent, schematic evolution of domain structure (after Ref. [32]).

the domains are aligned randomly. Consequently, unpoled ferroelectric ceramics do not exhibit macroscopic polarization or piezoelectricity. Small alternating (AC) electric fields, however, give rise to a vibration of the domain walls, which is associated with losses due to the emission of shear waves. Beyond a certain threshold field, *e.g.*, 16 V·mm^{-1} for barium titanate,[33] limited translation of domain walls sets in and the polarization increases linearly with field. This effect is generally referred to as 'reversible', that is, the effect on the principle domain structure is small and the initial configuration is recovered upon removal of the electric field as schematically shown in Figure 2.9.[3] If the electric field is further increased, unfavorably aligned domains will begin irreversible switching according to the electric field direction. Consequently, polarization increases rapidly in a nonlinear manner (II) until maximum alignment is reached. This is marked by increases in polarization (III), referred to as the saturation region. When the electric field is reduced some domains are found to switch back to their original configuration due to local electric and mechanical fields. A remanent polarization $P_{rem,+}$, however, remains at zero-field (IV). Due to the randomly aligned crystallites and their crystallographic axes, the remanent polarization is always smaller than the spontaneous polarization as measured in a single-domain single-crystal. For a tetragonal perovskite with its six available polar axes P_{rem} has a theoretical maximum of $0.83 \cdot P_s$.[6]

Upon further decrease of the applied electric field a reversal of polarization is found. At a negative field value $E_{c,-}$ the polarization reaches zero as some domains, previously aligned by the positive field, now began to align conversely with respect to the negative field (V). A further decrease of E yields negative polarization values and a reverse alignment of domains (VI). A subsequent increase

[3] Please note that, strictly speaking, this process is rather 'almost reversible'.

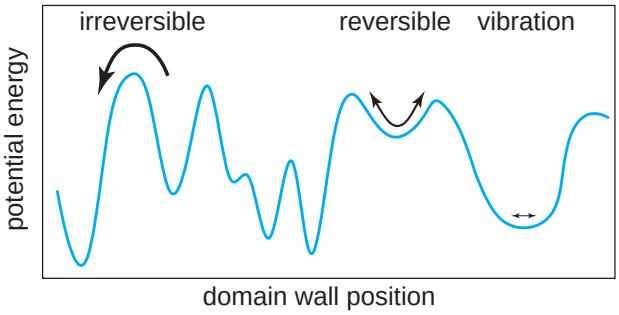

Figure 2.9: Schematic potential energy landscape of a domain wall in medium with randomly distributed defects (after Ref. [34]).

in E consequently leads to the negative remanent polarization $P_{rem,-}$ as well as a positive $E_{c,+}$. An ideal bipolar loop is symmetric, *i.e.*, $|E_{c,+}| = |E_{c,-}| = E_c$ and $|P_{rem,+}| = |P_{rem,-}| = P_{rem}$. The microscopic domain processes in polarization reversal are complex and involve several distinct mechanisms as nucleation and growth of new domains, growth of existing domains, and domain-wall motion. A sequence for polarization switching as proposed by Shur *et al.*[35] is presented by Figure 2.10. The triangular shape of newly emerging domains is the most favorable one because the resulting depolarization field is comparably small.[36] Note that the coercive field E_c is not constant but a function of different parameters such as frequency,[37] temperature,[38] or stress[39] (see also appended Figure A.1).

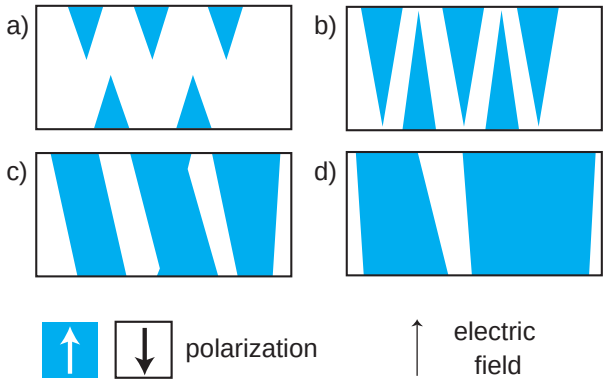

Figure 2.10: Sequence of polarization switching: a) nucleation of domains with reverse orientation, b) growth of these reverse domains, c) sideways motion of domain walls, and d) coalescence (after Ref. [35]).

As a consequence of both the intrinsic contribution, evolving from piezoelectricity, and the extrinsic processes, associated with domain switching, a strain is generated under the influence of an electric field. For bipolar cycling an $S(E)$ hysteresis is obtained as depicted by Figure 2.11. Due to the characteristic shape, this bipolar field-induced strain loop of ferroelectrics is referred to as a butterfly loop, where the 'wings' denote the polarization reversal. The term negative strain S_{neg} refers to the difference from the strain at zero-field to the minimum strain value.

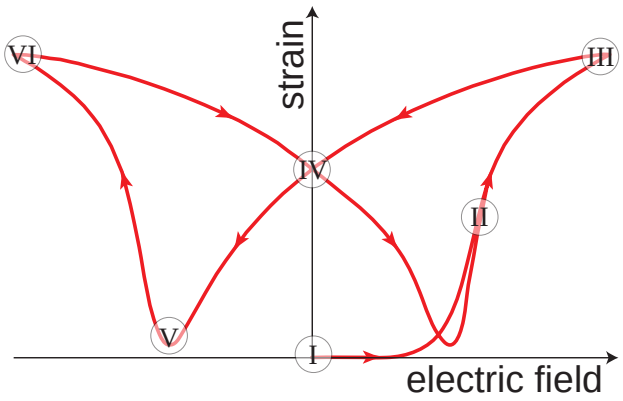

Figure 2.11: Schematic field-induced strain hysteresis obtained typically for ferroelectrics, also referred to as butterfly curve. Characteristic points are marked with (I) through (VI) in agreement with Figure 2.8.

2.1.3 Relaxor Ferroelectrics

Information within this chapter is based upon the review articles by Ye,[40] Samara,[41] Kleemann,[42], Bokov and Ye,[43] and Shvartsman and Lupascu.[44]

As the name suggests, relaxor ferroelectricity (RF) is closely related to conventional ferroelectricity (FE). Relaxor ferroelectrics are dielectrics, often crystallizing in an ABO_3 perovskite structure, capable of exhibiting strong piezoelectric coupling and large field-induced strains while their microstructure features polar regions, which are decisive for the functional properties. Despite these similarities, both groups of materials are inherently different in several aspects, as summarized by Figure 2.12.

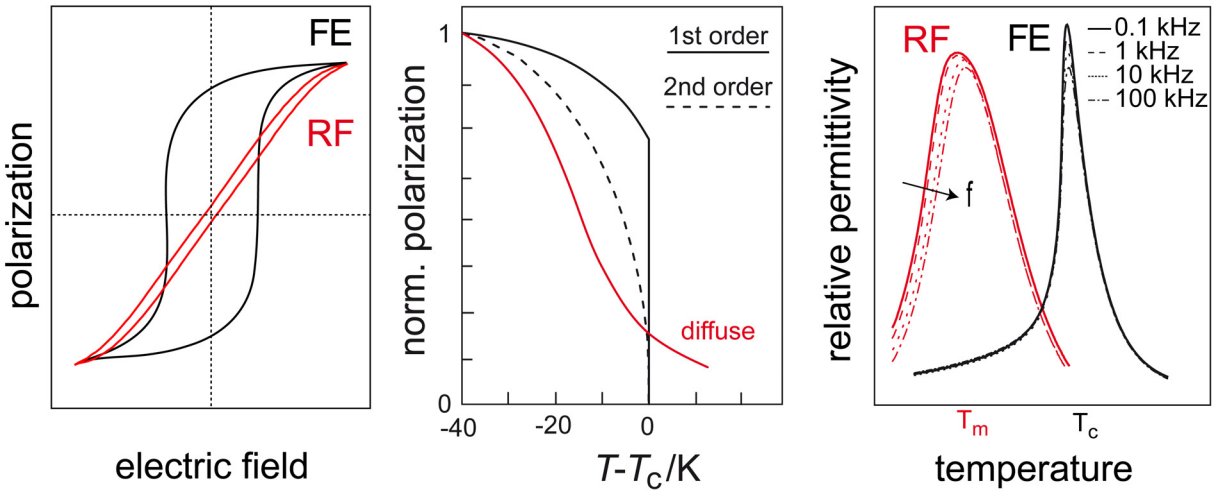

Figure 2.12: Comparison of ferroelectrics and relaxor ferroelectrics in terms of field-induced polarization (left), temperature-dependent polarization (middle), and relative permittivity (right) (after Ref. [41]).

In contrast to the rectangular polarization hysteresis observed for conventional FE, the $P(E)$ loops of RFs may remain slim with little remanence and minute 'coercive field'. Moreover, the temperature-driven FE-PE phase transition of ferroelectrics is associated with symmetry breaking and a peak in permittivity at T_c, above which the Curie-Weiss law applies and P_s=0. While the $\varepsilon'(T)$ curve of RFs also exhibits a maximum at temperature T_m, the values of both T_m and $\varepsilon'(T{=}T_m)$ depend on the measurement frequency. This effect, referred to as frequency dispersion, is one of the most characteristic features of RFs. In contrast to FE, this peak in permittivity is not associated with a structural phase transition and the permittivity does not obey the Curie-Weiss law for all $T{>}T_m$. Also, the remanent polarization may assume finite nonzero values in excess of T_m. Relaxor ferroelectrics, however, do not only stand out because of these properties but also due to their high applicability. Large dielectric constants are beneficial in capacitors, high electrostrictive coefficients are exploited in actuators and micropositioning, and the electro-optical characteristics are employed in devices such as shutters or optical modulators.

Although firstly reported in the mid 1950s by Smolenskii *et al.*[45,46] for $BaTiO_3$-$BaSnO_3$, the mechanisms behind relaxor ferroelectricity have not yet been fully understood. Currently, no single model is able to conclusively describe this phenomenon. Proposed models involve the diffuse phase transition model,[45] superparaelectric model,[47] dipolar glass model,[48] random field model,[49] breathing model,[50] random-bond–random-field model,[51] and the spherical random-bond–random-field model.[52] A comprehensive overview on the models is provided by Bokov and Ye.[43]

Despite the plethora of different models that attempt to deliver a concluding physical theory, there is little doubt about the importance of order-disorder and the existence of polar nanoscopic regions (PNR) in relaxors. The following section addresses order-disorder in complex perovskites, followed by descriptions of the temperature- and field-dependent behavior of relaxor ferroelectrics with respect to PNRs.

Order and Disorder in Complex Perovskites

Assuming a perovskite with mixed B-site, *i.e.*, $A(B'_{1/2}B''_{1/2})O_3$, each B-site ion should be located in its own respective sub-lattice in the compositionally ordered ground state. Since B' and B'' may be differently charged and with different ionic radii, the establishment of such a complete translational symmetry effectively reduces electrostatic and elastic energies. Thermal motion, however, is capable of destroying this ordering. Some complex perovskites exhibit a phase transition between the ordered and the disordered state at high temperatures, *e.g.*, $Pb(Sc_{1/2}Ta_{1/2})O_3$ (PST) or $Pb(Sc_{1/2}Nb_{1/2})O_3$ (PSN) at 1500 K.[53,54] By contrast, it is not possible to change the compositional disorder in other materials like $Pb(Fe_{1/2}Nb_{1/2})O_3$ (PFN) and $Pb(Mg_{1/3}Nb_{2/3})O_3$ (PMN) even by special annealing techniques; the relaxation time of the ordering, which involves diffusion of B' and B'' ions, is too high. This results in a quenched compositional disorder at low temperatures. This disorder, however, is not complete but inhomogeneous in nature, which gives rise to ordered regions that are embedded into a disordered matrix as a consequence of quenched phase fluctuations or incomplete order-disorder phase transformation. For PMN, a random-site model was suggested, according to which the first B-sublattice is occupied only by Nb^{5+} ions while the

second one comprises both Mg^{2+} and Nb^{5+} ions. Figure 2.13 illustrates schematically the inhomogeneous compositional order proposed for $Pb(B'^{2+}_{1/3}B''^{5+}_{2/3})O_3$ perovskites. Chemically ordered regions can be a source of strong electric fields due to the local charge imbalance.

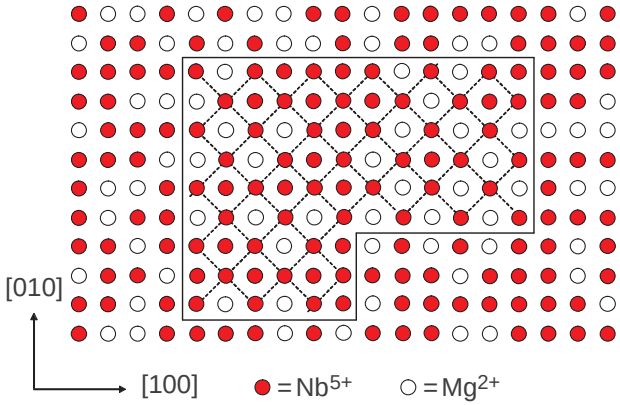

Figure 2.13: Ordered chemical nano-regions embedded into disordered matrix as suggested by the random-site model (after Ref. [43]).

It has been shown by different authors that compositional order-disorder may greatly affect the ferroelectric properties. For example, Setter and Cross[55] demonstrated that the degree of B-site order in PST can be controlled by heat treatment. A well-ordered single-crystal, obtained after long-time annealing at 1000 °C, exhibits a normal first-order ferroelectric phase transition and a corresponding spontaneous polarization. By contrast, a disordered sample shows a broad peak in $\varepsilon'(T)$ with strong dispersion, typical for relaxor ferroelectrics. Another example is $Pb(In_{1/2}Nb_{1/2})O_3$ (PIN). The disordered crystal, quenched from high temperatures, is a RF whereas the ordered crystal is antiferroelectric (AFE) with a sharp phase transition as evidenced by permittivity.[56] These examples support that relaxor ferroelectricity only occurs in disordered systems.

Random fields

The disorder in relaxor ferroelectrics bears some important implications in contrast to ordinary ferroelectrics. In FE a mean field approach can be applied to explain most properties, that is, any ion in the lattice is supposed to be subject to the same average field.[49] Below the transition temperature T_c ions are consequently shifted in a collaborative manner yielding a long-range order in the form of domains. In a disordered system, however, a distribution of random fields has to be assumed due to the presence of heterovalent lattice ions, defects, and impurities. Due to thermal fluctuations, no well-defined dipole moments can emerge at high temperatures. Upon cooling, however, dipolar entities arise. In a simple scenario of a dilute system, where these dipoles are not interacting, the relaxation response to an AC signal would be Debye-like and, therefore, could be described by a single relaxation time τ.

It has been shown, however, that random site electric dipoles may interact indirectly through the soft mode of a highly polarizable host lattice. A dipole on a certain lattice site may induce dipoles

in a region surrounding that site. Within the correlation length r_c the dipolar motion is consequently correlated, forming the earlier mentioned polar nano-region. Within the random-bond–random-field model the dipolar interactions are described by a model Hamiltonian according to Equation 2.17.[42]

$$H = -\sum J_{ij} I_i I_j - \sum h_i I_i \tag{2.17}$$

In this equation, the first term represents random bonds J_{ij} between dipole moments I_i and I_j while the second term represents quenched random fields h_i acting between dipolar moments I_i. Depending on whether random bonds or random fields dominate, the relaxor may undergo a spontaneous transition into a long-range ordered state or freezing into a glass-like state. Both scenarios will be explained in detail by means of temperature-dependent permittivity.

Temperature Dependence

The high-temperature paraelectric phase of FE and RF perovskites has a cubic average symmetry, *i.e.*, the non-centrosymmetric and non-polar point group $m\bar{3}m$. The ion configuration, however, can be slightly distorted as ions deviate from their respective crystallographic site of the ideal perovskite. For some lead-containing relaxors, *e.g.*, PMN, $Pb(Zn_{1/3}Nb_{2/3})O_3$ (PZN), and PIN,[43] it was reported that the Pb^{2+} ion exhibits uncorrelated displacements in a spherical layer with 0.03 nm radius around the ideal lattice site. In this high-temperature regime, the permittivity $\varepsilon'(T)$ obeys the Curie-Weiss law. As stated above, randomly distributed heterovalent ions and chemically ordered regions give rise to random fields, which promote the creation of polar nuclei whose polarity is determined by fluctuations of the random fields. The formation of these regions of polar symmetry is associated with additional electric and elastic fields around these regions, exerting a destabilizing effect. Therefore, there is no spontaneous net polarization at very high temperatures - the compound is paraelectric.

At a specific temperature, referred to as Burns temperature T_B in Figure 2.14, some nuclei become stable; they begin to form dynamic entities with a size above the critical size, *i.e.*, they do not disappear but grow in size. Note that the critical size in RFs can be as small as a few unit cells.[57] The Burns temperature T_B is determined as the temperature where deviation from the Curie-Weiss law occurs.[58] Close to T_B, the dipole moments of the PNRs are thought to be weakly correlated and capable of orienting freely. Consequently, the net average polarization $\sum P_i = 0$, meaning that there is no measurable remanent polarization; however, $\sum P_i^2 \neq 0$.[42] As a result, properties depending on P^2 are affected by the emergence of PNRs, such as electrostriction[47] and quadratic electro-optic effects as manifested in birefringence or second-harmonic generation (SHG).[59] Despite the lack of a structural change on a macroscopic or mesoscopic scale, this state is considered as a new phase for the dramatic changes in properties involved with the appearance of PNRs. Due to the mobility of the polar regions, the phase is referred to as an ergodic relaxor (ER) phase. The ergodicity is denoted in the system response after an external excitation, *e.g.*, the application of an electric field. Since the PNRs are free to rotate, the system subsequently returns to the same state of lowest free energy. This state does consequently not depend on the strength or polarity of the electric field.

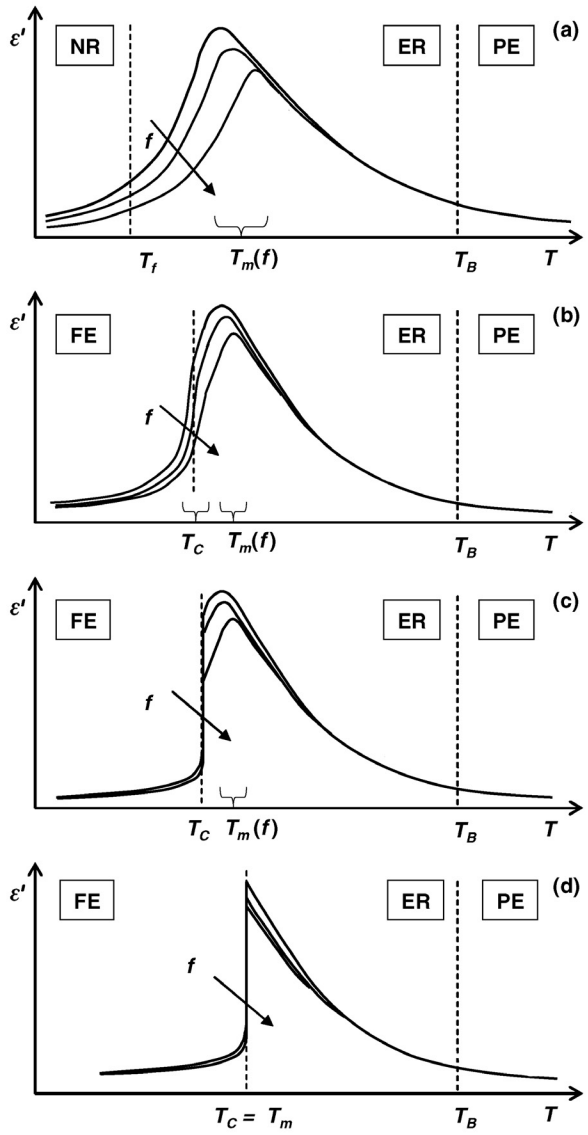

Figure 2.14: Temperature dependence of permittivity for a) canonical relaxor with freezing from an ER to a nonergodic relaxor (NR) state, b) crystal with a diffuse ER-FE phase transition at $T_c < T_m$, c) crystal with a sharp ER-FE phase transition at $T_c < T_m$, and d) crystal with a sharp ER-FE phase transition at $T_c = T_m$ (from Ref. [43]).

Upon further cooling below T_B, the PNRs grow in both number and size, which is attributed to the increased polarizability of the host lattice with decreasing temperature. For example, PNRs in PMN have a correlation length r_c of approximately 1.5 nm at T_B and 7 nm at 10 K,[60] while r_c in PZN increases from 7 nm to 18 nm at 300 K[61] as measured via high-resolution neutron elastic diffuse scattering. The increasing polar volume fraction upon cooling is reflected by increasing permittivity. From the increasing interaction among PNRs and their increasing size, however, there also arises a slowing down of their dynamics. The broad size distribution is associated with a broad distribution of relaxation times. As a consequence of the slowing down of the PNR dynamics and

the broadened relaxation time distribution, a frequency-dispersive maximum emerges with T_m denoting the temperature of maximum permittivity. As a natural implication of the relaxation processes, lower measurement frequencies yield a higher permittivity and a lower loss factor.

When the temperature is further decreased, two principle evolutions are possible. In the first case, the PNRs grow upon cooling. Eventually dynamic freezing sets in, resulting in a glass-like transition of the system. This state is referred to as nonergodic because the dipoles are strongly correlated and exhibit pronounced interactions among each other. Due to these interactions, some energy barriers in the free energy surface are too high to reach a state of overall lowest minimum free energy within reasonable laboratory times. Consequently, the system exhibits nonergodicity because thermodynamic averaging and time averaging yield different results. The freezing temperature T_f can be estimated by means of the Vogel-Fulcher law according to Equation 2.18.[62]

$$f = f_0 \cdot exp\left(-\frac{E_a}{k(T_m - T_f)}\right) \tag{2.18}$$

Here, f_0 represents an attempt frequency, E_a an activation energy, and k is the Boltzmann constant. It is important to note that no structural phase transition occurs across T_f, but the average symmetry remains nonpolar on a macroscopic scale. The correlation length of the PNRs, however, was found to increase significantly at T_f. At the same time, the number of PNRs decreases, which was suggested to be the result of small PNRs merging into larger ones. This class of so-called canonical relaxors include, for example, PMN, $Pb(Mn_{1/3}Ta_{2/3})O_3$ (PMT), and $(Pb_{1-x}La_x)(Zr_{1-y}Ti_y)O_3$ (PLZT) with high Lanthanum content. From this short-range ordered NR state, a long-range ordered FE state may be induced by both electric fields[63] or mechanical stress[64] as will be described later.

In the second scenario, the ergodic relaxor undergoes a spontaneous relaxor to ferroelectric phase transition upon cooling through T_c, which is at or below T_m, as illustrated by Figures 2.14 b)–d). This transition is associated with a clear symmetry breaking, *e.g.*, from cubic to tetragonal or rhombohedral. Moreover, micron-sized domains emerge, which can be imaged, for example, by means of piezoresponse force microscopy (PFM).[65] Electric properties, such as field-induced strain and polarization, are similar to normal ferroelectrics, *i.e.*, bipolar cycling yields a rectangular $P(E)$ loop and a butterfly-shaped $S(E)$ hysteresis. This relaxor-derived ferroelectric phase is indeed almost indistinguishable from conventional ferroelectrics. For PMN-PT, however, it was demonstrated that PNRs persist also in the FE phase and that micron-sized areas of average cubic symmetry coexist with the polar FE phase.[66] Moreover, compared to conventional FEs, the domain walls in RFs were shown to be more diffuse[67] and the dielectric response around the peak in $\varepsilon(T)$ is mainly governed by relaxation polarization instead of the phonon contribution through softening.[68] Therefore, the FE phase of relaxors must be discriminated from conventional FEs.

Field Dependence

A salient characteristic of the nonergodic relaxor phase is the electric field-induced transition from the relaxor to the ferroelectric phase, provided the applied electric field surpasses a threshold. The external electric field acts as a driving force, so that the quenched random electric fields

are overcome and micron-sized, long-range ordered domains can form from PNRs. Interestingly, according to Fu *et al.*,[69] the micron-sized domains in PMN were observed to possess a substructure consisting of elliptical PNRs of approximately 20 nm size coexisting with chemically ordered regions of 5 nm size.

The field-induced transition may occur either by application of an electric field during cooling from the ergodic phase (field cooling, FC) or by the application of an electric field after zero-field cooling (ZFC). Moreover, the transition involves a symmetry breaking, for example, pseudocubic PLZT 8.2/70/30 is turned into an orthorhombic phase[70,71] while PMN becomes rhombohedral,[72] which is observable by splitting in the respective diffraction patterns. Furthermore, the symmetry of the field-induced FE phase reflects the symmetry of the PNRs. The kinetics of the transition necessitates an incubation time between the electric field application and the onset of the transition. Thereby, the incubation time depends not only on temperature but also on the electric field, as shown in Figure 2.15.[73]

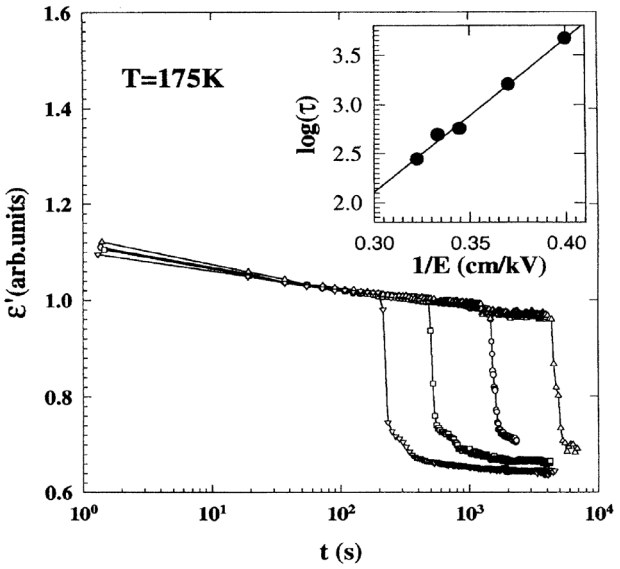

Figure 2.15: Time-dependent permittivity of PMN at 175 K under various electric bias fields (Ref. [73]).

After the removal of the electric field, the field-induced ferroelectric phase and polarization are metastable down to low temperatures. Upon zero-field heating (ZFH) above a T_{c0}, however, the long-range ordered state is again destroyed as a phase transition into the ergodic phase is found, which is also connected with the disappearance of ferroelectric domains.[74] It is important to note that T_{c0} is not related to T_m, which originates from the slowing down of PNR dynamics. Instead, it was found for some canonical relaxors, such as PMN, PSN, PST, and PMN-PT, that T_{c0} may be estimated from T_f as determined from fitting $T_m(f)$ using the Vogel-Fulcher equation.

In contrast to T_{c0}, which denotes the FE to ER transition temperature during ZFH, the temperature T_c for field-heating (FH) is not constant but a function of the electric field as demonstrated for PMN (see Figure 2.16).[63]

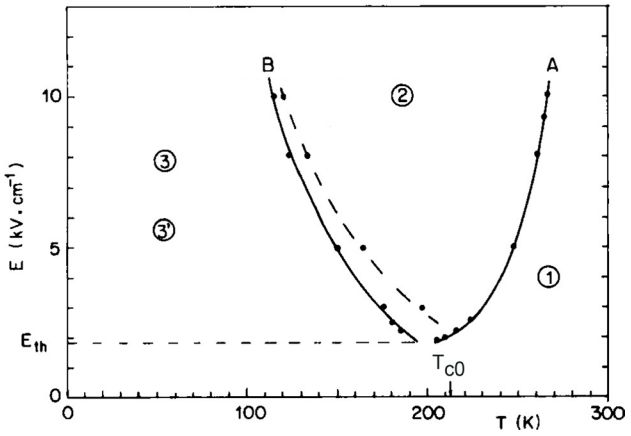

Figure 2.16: Electric field vs. temperature phase diagram as proposed for PMN: (1) pseudocubic ER, (2) induced FE phase of trigonal symmetry with reversible polarization, (3) pseudocubic NR state after ZFC, or (3)' induced trigonal phase (from (2)) with non-reversible polarization (after Ref. [63]).

Similar to conventional ferroelectrics the phase transition temperature is shifted to higher values with increasing electric field. Another E-T–diagram was reported for the likewise canonical relaxor PLZT 9/65/35, where a temperature dependence of the critical field was also found.[75] The reported phase diagram depends on the measurement procedure, that is, whether temperature is increased under constant electric field or *vice versa*. Also, the field required for the RF to FE transition is lower during FC from the ergodic phase compared to applying a voltage after ZFC.

Controversial Aspects in Relaxor Ferroelectrics

As previously stated, many details in the discussion of the peculiar features displayed by relaxor ferroelectrics are still subject to a controversial debate.

The most discussed topic is the glass-like behavior and the role of the cubic matrix. Classically, the PNRs are thought to be embedded into a cubic matrix, behaving similarly to dipolar glasses. Within the random-field approach, however, it is assumed that low-symmetry nano-domains form throughout the whole sample volume, meaning that the cubic phase does not separate the polar regions. One of the main arguments in favor of the domain image are Barkhausen jumps reported by Westphal *et al.*[76] for the poling of PMN, excluding glassiness. The two cases are compared in Figure 2.17. They can hardly be differentiated by experiment since the local symmetry of the pseudocubic phase is most likely not cubic and the thickness of the domain walls, where polarization is not well-defined, is on the order of the domain size.[43]

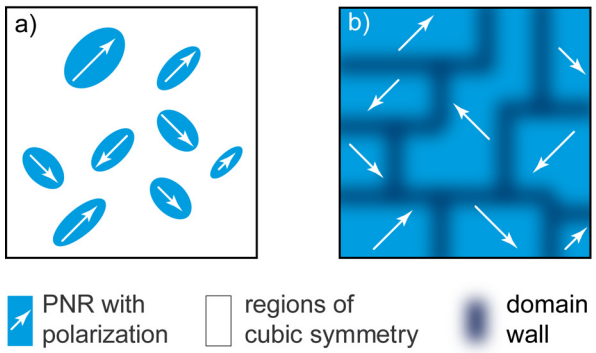

Figure 2.17: Comparison of different models: elliptical PNRs embedded into cubic matrix (a) in contrast to polar nano-domains (b) (after Ref. [43]).

Using a phase field model Kholkin *et al.*[77] demonstrated that an increasing number of defects and consequently augmented random fields yield a roughening of the domain walls. Eventually the increasing disorder causes a collapse into a chaotic order of small domains, as illustrated by Figure 2.18.

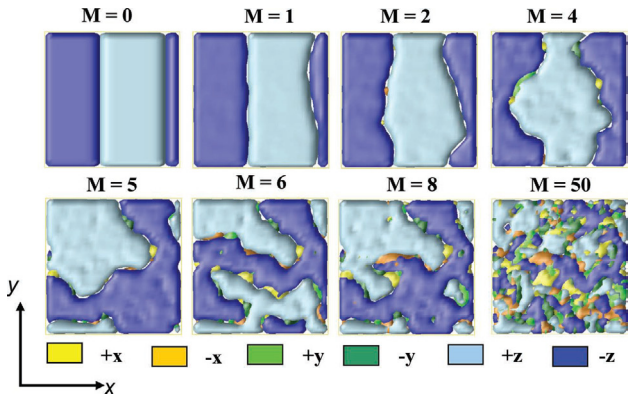

Figure 2.18: Evolution of domain structure with increasing disorder (here parameter M) as computed by phase field modeling (Ref. [77]).

Thus, the hypothesis of polar nano-domains depicted by Figure 2.17 b) is corroborated. Wang *et al.*[78] likewise used a phase field modeling approach considering the defects and came to the same result. They concluded from temperature-dependent calculations that a precursory state exists that is denoted by partial nonergodicity, *i.e.*, static domains appear at temperatures higher than the freezing temperature T_f. Also, for low defect concentrations PNRs are found to be embedded into much larger ferroelectric domains. Within this work, however, the term polar nano-region (PNR) will be used without implying the falsity of one or the other image pictured in Figure 2.17.

In addition, the existence of the Burns temperature T_B is still under discussion. Bobnar *et al.*[79] argued that PNRs are forming continuously due to the absence of any indication for such a specific

onset in fitted permittivity data of PMN-PT. The report stimulated a direct response of Scott,[80] which, however, did not provide any further argument for or against the existence of T_B.

A final question concerns the order of the field-induced phase transition in canonical relaxors. In PMN, the transition is of first order at moderate fields, but at high fields the transition is found to be of second order. In the case of PLZT 6/65/35 a first order transition is reported even though the parental PZT 65/35 composition exhibits a second order transition. Moreover, it is sometimes argued that 'field-induced ferroelectricity' is a contradiction in itself because ferroelectricity requires by definition the occurrence of a spontaneous polarization. Strictly speaking, spontaneity excludes the necessity for the application of an electric field.

None of the above-mentioned questions are the focus of the present work. The reader should be aware that a concluding theory and terminology in the field of relaxors has not yet been established.

2.2 $Bi_{1/2}Na_{1/2}TiO_3$-Based Lead-Free Piezoceramics

2.2.1 Bismuth Sodium Titanate

Small- and Large-Signal Properties

Discovered by Smolenskii *et al.* in 1961,[81] bismuth sodium titanate $Bi_{1/2}Na_{1/2}TiO_3$ (BNT) is not only the base compound for a whole family of BNT-derived lead-free piezoceramics but also offers a range of peculiar features as well as good electromechanical properties. In general, BNT is considered to be hard to pole, which was attributed mainly to the evaporation of bismuth during the sintering, giving rise to an increased oxygen vacancy density and consequentially elevated conductivity.[82] By using hot pressing or conventional sintering with excess of Bi_2O_3 dense ceramics can be obtained. The small-signal piezoelectric properties of 97 % dense BNT are summarized in table 2.2. The permittivity in this table and in the following is always provided for a frequency of 1 kHz if not stated otherwise. The parameter k_{33} is the coupling factor for a longitudinal oscillation. In general, coupling factors are nondimensional coefficients that describe the conversion of stored energy to mechanical or electric work. Other coupling factors are k_t for an oscillation along thickness direction or k_p for the radial oscillation of a thin plate.

Table 2.2: Small-signal properties of BNT (after Ref. [83])

parameter	value	unit
relative permittivity $\varepsilon_{r,33}$	583	
coupling factor k_{33}	0.459	
piezoelectric constant d_{33}	72.9	$pC{\cdot}N^{-1}$
elastic compliance s_{33}^E	8.32	$10^{-12}m^2{\cdot}N^{-1}$
elastic compliance s_{33}^D	6.57	$10^{-12}m^2{\cdot}N^{-1}$

Reports on the large-signal properties vary, as best exemplified by Takenaka who reported a coercive field E_c of 7.3 kV·mm^{-1} and a remanent polarization P_{rem} of 0.48 C·m^{-2} in 1990[84] but stated notably different parameters in 1999 with E_c=3 kV·mm^{-1} and P_{rem}=0.17 C·m^{-2}.[85] Other reports seem to confirm rather the former values.[86,87] The attainable maximum strain S_{max} during unipolar cycling is reportedly low with only 0.09 % under an electric field of 7 kV·mm^{-1}.[88] The fabrication of BNT thin films by means of radio-frequency magnetron sputtering was reported to yield a remanent polarization of 0.12 C·m^{-2}, a coercive field of 3.8 kV·mm^{-1}, and a relative permittivity on the order of 550 at 1 kHz.[89]

Structure of $Bi_{1/2}Na_{1/2}TiO_3$

In the first paper by Smolenskii *et al.*,[81] the structure was determined by means of X-ray diffraction as a cubic perovskite with a lattice parameter of 3.88 Å, which was later confirmed.[90] From neutron diffraction patterns, however, a rhombohedral phase was concluded with a phase transition at 280 °C into a tetragonal phase.[91] Jones and Thomas[92] provided further supporting evidence by means of Rietveld refinement of neutron diffraction (NRD) patterns, according to which BNT is rhombohedral with the space group $R3c$ possessing an antiphase oxygen octahedral tilting. This oxygen tilting system, $a^-a^-a^-$ in Glazer notation, causes a doubling of the unit cell that is associated with the occurrence of superlattice reflections corresponding to rhombohedral symmetry.[93] In the range of 250 °C to almost 400 °C, the tilting system changes to in-phase $a^0a^0c^+$ oxygen octahedra tilts, denoting a phase transition to a tetragonal $P4bm$ phase. Furthermore, an endothermic maximum in differential scanning calorimetry (DSC) at approximately 300 °C, a hysteresis in $\varepsilon_{r,33}(T)$, and a change in the coefficient of thermal expansion were observed in that temperature range.[94]

The structure as well as the polar nature of BNT, however, is still under debate. A high-resolution single-crystal XRD study suggested that the average structure may have lower than rhombohedral (Cc) symmetry,[95] which is supported by further experimental data by high-resolution powder XRD.[96] Additional transmission electron microscopy (TEM) studies uncovered a complex local structure with both tilting systems, $a^-a^-a^-$ and $a^0a^0c^+$, coexisting throughout a broad temperature range with tetragonal platelets embedded into a rhombohedral matrix.[97] Recently, Levin and Reaney[98] confirmed by TEM that BNT exhibits sizable disorder in terms of cation displacement, tilt, and ion distribution. According to the authors, BNT consists of nanoscopic twin domains with $a^-a^-c^+$ tilting and a size of <20 nm. Averaging, like in XRD or NRD experiments, yields pseudo-rhombohedral $a^-a^-a^-$ and average monoclinic $a^-a^-c^-$ tilting. Moreover, lattice disorder and the existence of nanoscopic polar regions is in line with broad phonon spectra in Raman scattering and frequency-independent dielectric losses at cryogenic temperatures.[99] According to Raman studies[100] the hybridization of the Bi $6s^2$ lone pair and the oxygen p-orbitals play a crucial role in the field- and temperature-dependent evolution of properties, while neutron pair-distribution demonstrated that Bi^{3+} exhibits different polar displacements.[101]

Relaxor Nature

BNT exhibits a well-known frequency dispersion observed during temperature-dependent permittivity measurements.[102] The temperature of maximum permittivity T_m was, however, found to be not directly correlated to a structural phase transition. Therefore, it was suggested that BNT bears similarity with the relaxors PLZT and PMN.[102] Accordingly, it was concluded from X-ray and neutron diffraction measurements that polar regions exist and grow upon cooling.[91] This assumption was further supported by measurements of the pyroelectric current,[103] where weak current pulses were rationalized with small polar regions. Moreover, the time-dependent evolution of permittivity was attributed to the existence of PNRs.[104] Anomalies in the Brillouin spectrum with regard to hypersonic velocity and damping were interpreted by Siny *et al.*[105] as disorder on the A-site lattice, which is also in accordance with the relaxor hypothesis. The same authors found broad Raman bands, which were rationalized with small polar regions in a cubic phase.[106] TEM measurements suggested that rhombohedral regions are divided by twinning planes that are effectively sheets with a $Pnma$ symmetry.[107] This assumption is in line with energy calculations by Gröting *et al.*[108] suggesting that chemically ordered, polar regions of nanoscopic size are embedded into chemically disordered regions. According to the computation, the chemically ordered regions may occur either as ellipsoids or as planar stacking faults.

2.2.2 $Bi_{1/2}Na_{1/2}TiO_3$-Based Pseudobinary Compositions

A number of BNT-based solid solutions have been investigated in an attempt to improve both sintering and electromechanical properties, particularly decreasing the high coercive field and increasing the attainable strains under low and high electric fields. Some of the most important pseudobinary systems will be briefly introduced in the following section.

$Bi_{1/2}Na_{1/2}TiO_3$ Modified with Strontium Titanate (BNT-ST)

One of the first and most thoroughly investigated pseudobinary BNT-based systems is BNT modified by strontium titanate, (1-x)BNT-$x$$SrTiO_3$ (BNT-100xST). The addition of $x$$SrTiO_3$ (ST) to BNT effectively decreases the electric field required to obtain saturated $P(E)$ loops, for example, 0.85BNT-0.15ST yields a P_{max} of 0.27 $C{\cdot}m^{-2}$ at 4.4 $kV{\cdot}mm^{-1}$.[109] At elevated temperatures a double hysteresis loop is observed that was rationalized with the occurrence of an 'AFE' phase. Moreover, ST decreases the temperature T_m of the maximum permittivity ε_m in the $\varepsilon(T)$ measurement. T_m is diminished linearly from approximately 340 °C for x=0 to almost room temperature for x=0.5. The proposed phase diagram consists of a FE to 'AFE' and an 'AFE' to PE phase transition, whereas both temperatures decrease with ST content.

More recently it was found that strontium titanate induces relaxor ferroelectric properties for $x{\geq}0.26$.[110] The frequency dispersion in $\varepsilon_{r,33}(T)$ is more pronounced with higher ST content, while the already only small non-cubic distortion is diminished. At the same time the polarization loop becomes slim and the remanent polarization decreases with x. It was also shown that the observed $P(E)$ loops are not saturating at fields as high as 6 $kV{\cdot}mm^{-1}$.

A report by Hiruma *et al.*[111] suggested the existence of a morphotropic phase boundary (MPB) at $0.26 \leq x \leq 0.28$, separating the rhombohedral and the pseudocubic phase. For x=0.28 a large unipolar strain was attained, *e.g.*, 0.2 % at 3 kV·mm^{-1}, yielding a normalized strain $S_{max} \cdot E_{max}^{-1}$ of approximately 665 pm·V^{-1}. The peculiar large-field behavior was hypothesized to result from polar micro regions. According to a TEM and IR spectroscopy study these micro-regions in BNT-ST are caused by the local ordering of A-site cations.[112] The local ordering gives rise to local inhomogeneities and eventually the creation of long-ranged ordering is impeded.

Phonon anomalies in temperature-dependent Raman measurements suggested a decrease in transition temperatures as well as strong relaxor properties for $x \geq 0.2$, which was further accompanied by a strong enhancement of room temperature permittivity with respect to unmodified BNT.[113] In accordance with supplementary XRD data, a phase diagram was proposed with an MPB at $x \approx 0.2$ where the split in the $\{111\}_c$ reflection vanishes, *i.e.*, the material is pseudocubic.

Another XRD study did not find evidence for the existence of such an MPB.[114] Instead, the enhanced electromechanical strain was suggested to originate from a field-induced AFE-FE transition. In contrast to former reports,[111] however, the normalized strain at low fields was considerably lower, *e.g.*, $S_{max} \cdot E_{max}^{-1}$ was as small as 250 pm·V^{-1} at 3 kV·mm^{-1}.

$Bi_{1/2}Na_{1/2}TiO_3$ Modified with Barium Titanate (BNT-BT)

After the first research articles on BNT-ST in 1974, a great number of reports has emerged on BNT modified with barium titanate, owing to a similar electron configuration ($5p^6$) and ionic size (1.61Å) of the Ba^{2+} cation compared to Sr^{2+} ($4p^6$, 1.44Å).

The first investigation of (1-x)BNT-$x$$BaTiO_3$ (BNT-100xBT) was published by Takenaka *et al.*[115], reporting an MPB between x=0.06 and x=0.07 as deduced from dielectric and piezoelectric properties. It was shown that the MPB composition displayed a coupling factor k_{33} of 0.55 with a d_{33} of 125 pC·N^{-1} and an $\varepsilon_{r,33}$ of 580. According to XRD data, the MPB was claimed to separate a rhombohedral from a tetragonal phase. Even though the authors mentioned the relaxor character of the composition due to the mixed A-site, the introduced phase diagram featured only a ferroelectric, antiferroelectric, and paraelectric phase. Thus, it strongly resembled the phase diagram published before for BNT-xST by Sakata *et al.*.[109] The polarization measurement for x=0.05 yielded a P_{rem} of 0.2 C·m^{-2} but this value decreased to virtually zero when heated to 160 °C. Moreover, the $P(E)$ loop exhibited double loop-like behavior at this temperature.

Nearly a decade after the first report, the interest in BNT-xBT increased after several publications showed useful electrical properties. The composition $x \approx 0.06$ was reported to feature the highest piezoelectric coefficient d_{33}. The discrepancy in absolute values among these reports is notable, *e.g.*, d_{33} ranges from 110 pC·N^{-1} up to 180 pC·N^{-1} while T_d is once found at 87 °C and once at 150 °C.

In a powder XRD study of compositions in the range $0 \leq x \leq 0.10$, Ranjan *et al.*[121] found rhombohedral symmetry up to $x \leq 0.055$. In contrast to the aforementioned reports, however, it was demonstrated that the rhombohedral tilt angle was zero for $x \geq 0.06$, *i.e.*, the initial rhombohedral

Table 2.3: Overview on properties of BNT-100xBT. R/T denotes a rhombohedral and tetragonal phase mixture.

parameter	Takenaka *et al.*[115]	Chu *et al.*[116]	Xu *et al.*[117]	Chen *et al.*[118]	Xu *et al.*[119]	Zhang *et al.*[120]	unit
composition x	0.06	0.06	0.06	0.07	0.06	0.06	
coupling	k_{33}=0.55	k_p=0.29	k_p=0.28	k_p=0.26	k_p=0.367	k_p=0.29	
d_{33}	125	122	180	176	155	110	pC·N^{-1}
T_m	290	225	n/a	240	290	242	°C
T_d	150	100	n/a	87	129	124	°C
P_{rem}	0.2	0.4	0.37	0.378	0.388	0.34	C·m^{-2}
E_c	n/a	2.88	4.27	2.72	3.41	2.6	kV·mm^{-1}
structure	R/T	R/T	R/T	R/T	R/T	n/a	

distortion vanishes. Lacking a clear evidence for tetragonal splitting, the authors consequently described the structure as nearly cubic. The finding of an apparently non-polar symmetry is peculiar and contrasts the observation of macroscopic piezoelectricity. In subsequent XRD experiments on BNT-7BT it was found that the application of high electric fields triggered a phase transition and induced sizable tetragonal distortions as well as the establishment of a domain structure.[122] From neutron diffraction experiments on BNT-6BT Simons *et al.*[123] likewise concluded a field-induced transition, although into a predominantly rhombohedral phase.

Owing to the good electromechanical properties and the peculiar phase change behavior, BNT-100xBT has consequently become the most widely studied BNT-based model material system with numerous experimental techniques employed to gain further insight. A variety of phase diagrams has been proposed by different authors. Raman scattering suggested the MPB between x=0.05 and x=0.06.[124] For x>0.055 no structural phase transition was observed. Instead, the high-temperature phase with short-range ionic displacements resembled the long-range ordered phase at room temperature. Moreover, poling apparently moved the MPB to higher x values. According to TEM studies, the MPB cannot only be moved but also created.[125] Application of an electric field was shown to yield a $R3c/P4bm$ MPB and, therefore, the piezoelectric coefficient was augmented. It was also demonstrated that the microstructure varies with x as ferroelectric domains of approximately 100 nm size are replaced by nanoscopic regions for $x \geq 0.07$.[126] The field-induced evolution of the MPB was furthermore corroborated by *in situ* XRD experiments in combination with small-signal measurements as presented by Jo *et al.*.[127] Application of an electric field changed the MPB into an MPB-region with both rhombohedral and tetragonal phase fractions. Subsequent dielectric measurements and the deconvolution thereof suggested the existence of PNRs of both symmetries.[128]

$Bi_{1/2}Na_{1/2}TiO_3$ Modified with Bismuth Potassium Titanate (BNT-BKT)

The pseudobinary BNT-100xBKT system incorporates the tetragonal endmember $Bi_{1/2}K_{1/2}TiO_3$ (BKT).[81,90] The first study on BNT-100xBKT was conducted by Elkechai *et al.*[129] who found a region of coexisting rhombohedral and tetragonal phases for $0.08 \leq x \leq 0.3$ and first small-signal measurements suggested that piezoelectric properties are enhanced for these compositions. This assumption was substantiated by the finding of coupling factors and piezoelectric constants peaking for $0.16 \leq x \leq 0.2$.[130] Temperature-dependent measurements yielded a depolarization temperature of 174 °C, which is notably higher than for BNT-6BT and supported by subsequent work, as presented by Table 2.4.[131]

Table 2.4: Characteristic small- and large-field properties for BNT-20BKT.

parameter	Sasaki *et al.*[130]	Yoshii *et al.*[131]	Hiruma *et al.*[132]	unit
relative permittivity $\varepsilon_{r,33}$	1030	884	930	
coupling factor	k_p=0.27	k_{33}=0.54	k_{33}=0.54	
piezoelectric constant	d_{31}=46.9	d_{33}=157	d_{33}=167	$pC \cdot N^{-1}$
depolarization temperature T_d	n/a	174	175	°C
elastic compliance s_{11}^E	8.81	11.0	n/a	$10^{-12} m^2 \cdot N^{-1}$
remanent polarization P_{rem}	0.199	0.384	n/a	$C \cdot m^{-2}$
coercive field E_c	3.0	3.6	n/a	$kV \cdot mm^{-1}$

The frequency dispersion in $\varepsilon(T)$ known from unmodified BNT also persists in BNT-BKT, suggesting a relaxor-like behavior rationalized with the A-site cation disorder.[133] This argumentation is corroborated by a combined XRD and Raman study that suggested the existence of nanometer-sized domains due to significant diffuse scattering in the diffraction pattern and a 135 cm^{-1} band in the Raman spectrum.[134] In a subsequent neutron diffraction study the initially rhombohedral $R3c$ phase of BNT-20BKT was demonstrated to be a rhombohedral and tetragonal phase mixture between 230 °C and 330 °C, purely tetragonal up to 700 °C, and eventually cubic.[135] By contrast, Anton *et al.*[136] recently reported that neutron and high-resolution X-ray diffraction patterns were best fit on the base of a tetragonal ($P4bm$) and monoclinic (Cc) phase mixture, while no indication for a phase transition was observed up to 500 °C. Also, the coexistence of lamellar domains and PNRs in BNT-20BKT was evidenced by TEM.

$Bi_{1/2}Na_{1/2}TiO_3$ Modified with Bismuth Zinc Titanate (BNT-BZT)

BNT modified with $BiZn_{1/2}Ti_{1/2}O_3$ (BZT) has received considerable attention due to the exceptionally large tetragonality c/a=1.211 and computed transition temperature T_c=1381 °C reported for the metastable compound BZT.[137,138] The addition of BZT to lead titanate (PT), for example, represents one of the rare cases where a modification of PT gives rise to an increase in T_c. This poses the question whether a similar effect can be observed in lead-free BNT and BNT-based systems.

Upon substitution with BZT both BT and BNT exhibit a decrease in T_c as well as an increase in grain size and density.[139] By contrast, it was later claimed that T_c increased upon addition of 2.5 mol% BZT from 290 °C to 310 °C.[140] Due to the absence of a defined way of determining T_d, the effect of BZT on depolarization temperatures cannot be presently clarified. Electromechanical properties were found to peak at x≈0.0375 with the respective properties listed in Table 2.5.

Table 2.5: Characteristic small- and large-field properties for BNT-100xBZT.

parameter	Zhang *et al.*[140]	Patterson *et al.*[141]	Zhang *et al.*[142]	unit
BZT content x	0.0375	0.04	0.04	
relative permittivity $\varepsilon_{r,33}$	800	750	960	
coupling factor	k_p=0.22	n/a	n/a	
piezoelectric constant	d_{33}=92	n/a	n/a	pC·N^{-1}
depolarization temperature T_d	<150	n/a	n/a	°C
maximum polarization P_{max}	0.42	0.35	0.30	C·m^{-2}
remanent polarization P_{rem}	0.365	0.3	0.23	C·m^{-2}
coercive field E_c	3.5	4.7	3.1	kV·mm^{-1}
normalized strain $S_{max}{\cdot}E_{max}^{-1}$	100	n/a	105	pm·V^{-1}

The finding of maximum properties at y=0.0375 was rationalized with the existence of a morphotropic phase boundary. A subsequent XRD study did not provide evidence of an MPB for $x \leq$0.2.[143] Instead, the synthesized compounds reportedly exhibit a small rhombohedral distortion that decreased upon adding BZT. Patterson *et al.*[141] likewise did not observe an MPB from XRD data, but rather a rhombohedral and tetragonal phase mixture up to 8 mol% BZT. BZT was found to induce a flattening and slimming of the $P(E)$ loops, *e.g.*, P_{rem} decreased from 35 C·m^{-2} in BNT-2BZT to 20 C·m^{-2} in BNT-8BZT while E_c decreased from 5.2 kV·mm^{-1} to 3.8 kV·mm^{-1}. Moreover, double-loop behavior emerged at elevated temperatures. The knowledge on BNT-BZT is further complemented by temperature-dependent measurements of strain performed by Zhang *et al.*[142] who observed an increase in $S_{max}{\cdot}E_{max}^{-1}$ from 105 pm·V^{-1} at room temperature to approximately 270 pm·V^{-1} at 130 °C, which is accompanied by a decrease in negative strain. According to Table 2.5, the properties of BNT-100xBZT are sensitive to changes in sample preparation as evidenced by the sizable variation of large-signal properties.

2.2.3 $Bi_{1/2}Na_{1/2}TiO_3$-Based Pseudoternary Compositions

The two material systems studied within this work are the pseudoternary BNT-BT-KNN and BNT-BKT-BZT. The former was developed based on reportedly morphotropic BNT-6BT by the addition of potassium sodium niobate $K_{0.5}Na_{0.5}NbO_3$ (KNN). First demonstrated by Zhang *et al.*,[144] low KNN content results in large strain under high electric fields and a vanishing of remanent and negative strain. With an $S_{max}{\cdot}E_{max}^{-1}$ of 560 pm·V^{-1} at 8 kV·mm^{-1}, BNT-6BT-2KNN surpassed even soft PZT under the same conditions. A later study in the compositional vicinity of BNT-6BT-2KNN confirmed that the electromechanical properties are highly sensitive to the composition.[145,146] A

Table 2.6: Overview on properties reported for ternary systems (1-x-y)BNT-xBT-yX. The footnotes in column d_{33}^* denote the employed electric field amplitude in kV·mm^{-1}.

X	x /%	y /%	d_{33} / pC·N^{-1}	coupling	$\varepsilon_{r,33}$	T_d / °C	P_{rem} / C·m^{-2}	E_c / kV·mm^{-1}	d_{33}^* / pm·V^{-1}	Ref.
KNN	6	2	30	n/a	2320	$\leq$25	0.16	1.3	567_8	[145,146]
	2.8	12	191	k_p=0.33	1141	n/a	n/a	n/a	n/a	[151]
	3.5	10	133	k_p=0.26	n/a	n/a	n/a	n/a	n/a	[152]
BKT	3.6	8	122	k_p=0.3	2200	n/a	0.344	3.65	188_8	[153]
	3.8	11	220	k_p=0.31	1648	157	0.334	2.78	n/a	[150]
	2.6	12	n/a	n/a	n/a	n/a	n/a	n/a	295_5	[154]
BZr	8.5	0.5	147	n/a	881	n/a	0.16	2.4	n/a	[155]
BAgT	6	5.4	168	k_p=0.31	920	180	n/a	n/a	n/a	[156]
BH	7.6	0.4	136	n/a	300	180	n/a	n/a	n/a	[157]
ST	6.5	22	9	n/a	2700	$\leq$25	0.04	0.5	490_4	[158,159]
BLT	6.0	7.5	208	k_p=0.368	1000	85	0.392	3.7	n/a	[160]

lower BT and/or KNN content yielded butterfly-shaped $S(E)$ loops and rectangular $P(E)$ loops, both being reminiscent of ferroelectric behavior. By contrast, higher BT and/or KNN contents induced the practically same behavior like in BNT-6BT-2KNN, *i.e.*, high maximum strain without negative strain and pinched $P(E)$ loops. The maximum values, however, were reduced with respect to BNT-6BT-2KNN. Since TEM showed no ferroelectric domains in the virgin state, the authors hypothesized that a reversible, field-induced transition between an 'AFE' and a FE phase takes place. By means of *in situ* diffraction[147] and TEM[148] it was indeed demonstrated that the application of an electric field triggers a phase transition from pseudocubic to rhombohedral with the consequential establishment of micron-sized domains. Jo *et al.*[149] reported that the large strain is associated with merely minute remanent strain and polarization, which supports the phase transition hypothesis and explains the lack of sizable small-signal d_{33} values. The nature of the phase transition is, however, still under debate. Other compounds (X) used in pseudoternary solid solutions (1-x-y)BNT-xBT-yX are BKT, $BaZrO_3$ (BZr), $Bi_{1/2}Ag_{1/2}TiO_3$ (BAgT), $BaHfO_3$ (BH), $SrTiO_3$ (ST), or $Bi_{1/2}Li_{1/2}TiO_3$ (BLT). Properties and related references are listed in Table 2.6. The focus in these BNT-BT based systems lies mainly on the small-signal properties, *i.e.*, high d_{33} and planar coupling factor k_p as demonstrated by BNT-3.8BT-11BKT with 220 pC·N^{-1} and 0.31, respectively.[150]

Similar to BZT-modified BNT, the second material system considered in this work, BNT-BKT-BZT, has recently gained increasing attention. Patterson *et al.*[161] investigated BNT-40BKT-100yBZT and found high strains with $S_{max}{\cdot}E_{max}^{-1}$ as high as 547 pm·V^{-1} for y=0.05. Similar to BNT-BT-KNN, the incorporation of the tertiary compound, here BZT, induced a decrease in maximum and remanent values as manifested in the constriction of the $P(E)$ loop. An increase in temperature had an analog effect on the large-signal response, *i.e.*, the polarization hysteresis exhibited a more pronounced constriction with decreasing remanent polarization and decreasing coercive field. Ullah *et al.*[162] found similar properties for compositions originating from the suppos-

Table 2.7: Overview on properties reported for ternary systems (1-x-y)BNT-xBKT-yX. The footnotes in column d_{33}^* denote the employed electric field amplitude in $kV{\cdot}mm^{-1}$.

X	x /%	y /%	d_{33} / $pC{\cdot}N^{-1}$	coupling	$\varepsilon_{r,33}$	T_d / °C	P_{rem} / $C{\cdot}m^{-2}$	E_c / $kV{\cdot}mm^{-1}$	d_{33}^* / $pm{\cdot}V^{-1}$	Ref.
BZT	40	5	n/a	n/a	n/a	n/a	0.07	0.8	547_6	[161]
	18	3	166	k_p=0.317	1400	n/a	0.23	3.0	270_7	[162]
	18	7	11	n/a	1200	n/a	0.07	1.2	385_7	[162]
BA	15	5	62	n/a	4139	n/a	0.13	2.5	276_7	[163]
	22	3	n/a	n/a	1800	n/a	0.08	1.1	592_6	[164]
BNiT	20	5	n/a	n/a	n/a	n/a	0.04	0.9	520_5	[165]
BMT	22.5	5	n/a	n/a	n/a	n/a	0.06	1.0	570_5	[165]
ST	20	5	n/a	n/a	2400	14	0.046	0.8	600_6	[166]
BLA	22	1	n/a	n/a	n/a	n/a	0.09	1.1	579_7	[167]
BC	21	1	156	k_p=0.34	1200	n/a	n/a	n/a	n/a	[168]
KNN	20	1	n/a	n/a	n/a	n/a	0.06	0.8	575_8	[169]
BLT	25	5	145	k_p=0.221	1276	n/a	n/a	n/a	n/a	[170]
BCr	18	1.5	168	k_p=0.32	1730	n/a	n/a	n/a	n/a	[171]
BAgT	79	1	160	k_p=0.3	1110	94	0.288	2.72	n/a	[172]
BF	18	3	170	k_p=0.366	890	n/a	n/a	n/a	n/a	[173]

edly morphotropic composition BNT-18BKT. While 3 % BZT yielded a high d_{33} of 166 $pC{\cdot}N^{-1}$, the normalized strain $S_{max}{\cdot}E_{max}^{-1}$ was higher for 7 % BZT with 385 $pm{\cdot}V^{-1}$. Beyond BZT, a plethora of tertiary endmember compounds X had been employed in (1-x-y)BNT-xBKT-yX: $BiAlO_3$ (BA), $BiNi_{1/2}Ti_{1/2}O_3$ (BNiT), $BiMg_{1/2}Ti_{1/2}O_3$ (BMT), $SrTiO_3$ (ST), $Bi_{1/2}La_{1/2}AlO_3$ (BLA), $BiCoO_3$ (BC), $K_{0.5}Na_{0.5}NbO_3$ (KNN), $Bi_{1/2}Li_{1/2}TiO_3$ (BLT), $BiCrO_3$ (BCr), $Bi_{1/2}Ag_{1/2}TiO_3$ (BAgT), or $BiFeO_3$ (BF); properties and related references are listed in Table 2.7. Many of these BNT-BKT based systems are investigated mainly with respect to the exceptionally large strains with $S_{max}{\cdot}E_{max}^{-1}$ as high as 600 $pm{\cdot}V^{-1}$, though high electric fields are required for activation.

3 Concept and Aim

Lead-free BNT-based materials can exhibit large field-induced strains under certain conditions. Such a behavior would be useful for actuators that produce forces and displacements, for example, in fuel injectors, micro-pumps, or camera lenses. In addition, the large permittivity across broad temperature ranges is promising for high-capacity capacitors. In order to develop ceramics with the potential to replace lead zirconate titanate, a full understanding of BNT-based material systems is required. Some fundamental questions have not been to date sufficiently answered:

1. What is the underlying physical mechanism for the outstanding electromechanical properties found for some BNT-based compositions?
2. How does temperature affect the structural and functional properties and how are both interrelated?
3. What is the influence of mechanical loads on the field- and temperature driven processes?

No single technique is capable of providing a satisfactory answer to all three questions. Instead, a broad methodological approach is necessary to investigate the field- and temperature-dependent properties. In particular, it is important to investigate the evolution of functional properties, mechanical properties, crystal structure, and microstructure. Only a diverse methodology can elucidate the underlying mechanisms responsible for the peculiar characteristics of BNT-based lead-free piezoceramics. At the same time these measurements must address open questions of practical relevance:

1. Can large field-induced strains also be obtained at high frequencies and under large compressive loads?
2. Are BNT-based materials capable of producing large forces?
3. How good is the energy conversion efficiency?
4. Is it possible to create a dielectric with large, yet stable permittivity across a broad high-temperature range?

As discussed in Chapter 2.2, there are numerous BNT-based pseudobinary and pseudoternary material systems. BNT-100xBT-100yKNN is the most widely studied system and demonstrates intriguing field- and temperature-dependent properties.[144,174] Therefore, it acts as the model system within this work to study the field-, temperature-, and stress-dependent phenomena. The understanding gained from BNT-6BT-100yKNN is contrasted with the second lead-free system, BNT-100xBKT-100yBZT. This material has been recently developed and features a notably different chemistry.[175] As outlined earlier, BZT efficiently increases the phase transition temperature of

lead titanate and induces an extremely large tetragonal distortion.[176] It is investigated whether BZT has the same effect on BNT-BKT, which was chosen due to its favorable piezoelectric properties.

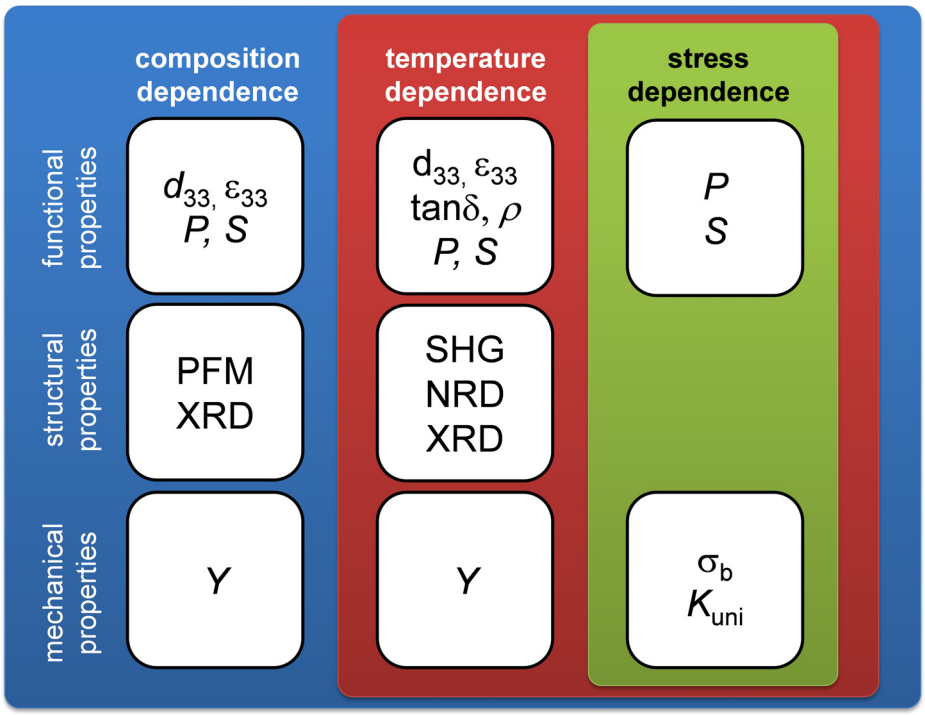

Figure 3.1: Concept and scope of this work. Please note that microstructure and crystal structure are here listed together as 'structural properties' for the sake of clarity.

The experimental concept of this work is schematically illustrated by Figure 3.1. The techniques mentioned here comprise the measurement of

- Large-field constitutive behavior of strain (S) and polarization (P),
- Small-signal properties permittivity (ε), loss factor (tanδ) and piezoelectric coefficient (d_{33}),
- Electrical resistivity (ρ),
- Blocking stress (σ_b),
- Elastic properties such as the Young's modulus (Y) and uniaxial compressive modulus (K_{uni}),
- The domain structure and its electric field dependence, assessed by means of piezoresponse force microscopy (PFM),
- The crystal structure, assessed by means of X-ray diffraction (XRD), neutron diffraction (NRD), and second-harmonic generation (SHG).

In Chapter 4 the composition dependence is investigated at room temperature. Then, temperature is introduced in Chapter 5 as an additional variable. Finally, the effect of stress is analyzed in Chapter 6, including variation of both composition and temperature. Each of these following three chapters includes a description of the employed methods, a listing of the results, a subsequent discussion, and finally a brief summary. The following chapter covers the practical implications of the results and a discussion with respect to applications. All findings are summarized and further discussed in Chapter 8.